UNIVERSIDAD DE CONCEPCIÓN
FACULTAD DE CIENCIAS FÍSICAS Y MATEMÁTICAS

Probing black hole formation via collisions in black hole clusters

Por: Benjamín Alfonso Gaete Diaz

Tesis presentada a la Facultad de Nombre de Facultad de la Universidad de Concepción para optar al grado académico de Magíster en Astronomia

Diciembre 2023
Concepción, Chile

Profesor Guía: Dominik Schleicher

En memoria a lunita que en paz descanse

AGRADECIMIENTOS

Primero quiero agradecer a mi familia, mi madre Carolina Diaz, mi padre Raúl Gaete, mis hermanos Gonzalo Gaete y Maximiliano Gaete por su apoyo incondicional, cariño y comprensión que siempre me han brindado en este difícil viaje, gracias a ellos he logrado este difícil objetivo.

A mis amigos y compañeros del magister que brindaron un gran apoyo y eventos de dispersión, ultimo y no menos importante gracias a mis amigos de toda la vida que aunque lejos también me dieron su apoyo.

También dar las gracias a mi profesor y supervisor Dominik Schleicher por el apoyo y sustento para poder realizar esta investigación. Finalmente agradecer proyecto CATA, por su soporte financiero a través de PROYECTO BASAL FB2100003 que recibí durante el programa de magíster.

Resumen

El origen de los agujeros negros supermasivos en centros galácticos a altos redshifts en el Universo temprano es aún desconocido. En las últimas décadas, astrónomos han propuesto un amplio rango de modelos para explicar la formación de estos objectos y su correlación entre sus masas y la de las galaxias que los hospedan. Algunas posibles explicaciones implican semillas muy masivas, acreciones de hyper-Eddington y supra-exponensial, super cúmulos masivos libre de metales, el colapso de las primeras estructuras bariónicas y la formación de SMBHs vía fusiones de agujeros negros. En este proyecto, estudiamos la formación de objectos supermasivos en cumulos nucleares (NSC, por su siglas en ingles) a través de la fusión de agujeros negros, además afectado por el pozo potencial de gas. Nosotros consideramos el efecto del potencial externo debido al gas y los efectos relativistas mediante efectos post-Newtonianos. El modelo fue investigado mediante simulaciones N-body usando el código Nbody6++gpu. Presentamos un total de 100 simulaciones, donde variamos tanto el potencial externo como la velocidad de la luz debido a su alto consumo computacional. El objetico es extrapolar los resultados al valor real de la velocidad de la luz. Nuestros resultados indican que el tiempo de core collapse en presencia de mayores potenciales externos de gas tiende a disminuir en cúmulos en estado relativista, en cambio para cúmulos fuera de un estado relativista, el comportamiento es distinto y el tiempo de core collapse tiende a aumentar a mayores potenciales de gas. Por otro lado, los IMBH formados se encuentran en 2 rangos de masas; los mas masivos con masas de $10^4 M_\odot$ para cúmulos en estados relativistas, donde la mayoría de las fusiones terminan en IMBH, y $10^3 M_\odot$ para cúmulos fuera de un estado relativista, donde la cantidad de fusiones que terminan siendo absorbidos por IMBH decrece substancialmente.

Keywords **–** IMBH - methods: numerical - theory

Abstract

The origin of SMBHs in galactic centers at high redshift in the early Universe is still unknown. In recent decades, astronomers have proposed a wide range of models to explain the formation of these objects and the correlation of their masses with the host galaxy. Some theoretical explanations include very large seed masses, hyper-Eddington or supra-exponential accretion, very massive metal-free superclusters, the collapse of the first baryon structures, and the formation of SMBHs via BH mergers. In this project, we examine the formation of massive objects in the nuclear star cluster (NSC) core through the fusion of black holes. We consider the effect of an external gas potential and post-Newtonian corrections in our study. The model is investigated via N-body simulations using the Nbody6++gpu code. We present the results of 100 simulations, where we vary the mass of the gas potential. Since the simulations are computationally expensive when considering the real speed of light, we treat it as a free parameter and determine results assuming different speeds of light, with the aim of extrapolating our results to the physical value. Our findings indicate that the time of core collapse in the presence of higher external gas potential tends to decrease in relativistic clusters. For clusters out of the relativistic state, the trend is completely different, tending to increase at higher external potential. On the other hand, the BH seeds that form are set in two ranges: $\approx 10^4 M_\odot$ for clusters in relativistic states, where almost all BH mergers end in the BH seed, and $\approx 10^3 M_\odot$ for clusters out of the relativistic state, in this case only a few percent of mergers end in the BH seeds.

Keywords **–** IMBH : formation - methods: numerical - theory

Contents

List of Tables

List of Figures

Chapter 1

Introduction

1.1 Introduction

The existence of supermassive black holes (SMBHs) and their physical nature has been confirmed through different independent observations, including the orbits of the S2 stars near the center of Milky Way with the GRAVITY instrument (GRAVITY Collaboration et al., 2018), as well as the observation of their shadows at the centers of M87 and Sagitarius A* (Event Horizon Telescope Collaboration et al., 2019, 2022). Observed through the detection of Active Galactic Nuclei (AGN) at high redshift (e.g. Shankar et al., 2010), even at redshifts larger than $z > 6$, more than 200 quasars have been detected (e.g. Bañados et al., 2016; Inayoshi et al., 2020). These objects are very rare with number densities of $\sim 1\ \mathrm{Gpc}^{-3}$ and have so far been found in optical/infrared(IR) surveys that cover a large portion of the sky, such as the Sloan Digital Sky Survey (SDSS), the first survey to discover a high-redshift quasar (Fan et al., 2001).These objects SMBHs are common in the centers of local galaxies (e.g. Ferrarese and Merritt, 2000; Tremaine et al., 2002; Gültekin et al., 2009). Their masses are in the range of $10^6 - 10^{10} M_\odot$.

The most distant quasar detected so far is ULAS J1342+0928 with a redshift of $z = 7.54$ which is SMBH mass of $\approx 8 \times 10^8 \mathrm{M}_\odot$ (Bañados et al., 2018). In the local Universe the rarest SMBHs are the so-called ultra-massive ones; over the last decade observations have established the existence of a few of these with masses $\gtrsim 10^{10} \mathrm{M}_\odot$ in some bright cluster galaxies (e.g. McConnell et al., 2011;

Hlavacek-Larrondo et al., 2012; Wu et al., 2015).

In the local Universe, galaxies were also found to host nuclear star cluster (NSCs) at their center (Neumayer et al., 2020). The most massive NSCs are the densest known stellar systems and can reach mass surface densities of $\approx 10^6 M_\odot/pc^2$ or higher. Some important features of these objects and an important topic to study are their correlations with their host galaxies, such as the tight correlations with the masses of their host galaxy (Wehner and Harris, 2006; Rossa et al., 2006; Ferrarese et al., 2006).

There are a number of cases where nuclear stars cluster and massive black holes were found to co-exist (Filippenko and Ho, 2003; Seth et al., 2008; Graham and Spitler, 2009; Neumayer and Walcher, 2012; Nguyen et al., 2019). Other nearby examples of SMBH detections within NSCs are M31 (Bender et al., 2005), M32 (Verolme et al., 2002; Nguyen et al., 2018), NGC 3115 and the Milky Way (Tonry, 1984; Dressler and Richstone, 1988; Richstone et al., 1990; Kormendy and Richstone, 1992; van der Marel et al., 1994). The co-existence suggests that the build-up of NSC and the growth of massive black holes are closely related (see also Escala, 2021; Vergara et al., 2022).

The high masses of the SMBHs at an early age of the Universe where we observe these objects are a real challenge for the formation theories of these objects. If we assume super-Eddington accretion with only 10% of the matter falling into the black hole being radiated away, a stellar-mass black hole with a mass of $= 10\ M_\odot$ requires a timescale of $t_{accr} \approx 1$ Gyr to reach the masses of SMBHs observed in the most massive AGN. However, it is unlikely to grow so much because the removal of the gas reservoir by UV radiation and supernova (SN) explosions of the Pop III stars in the shallow gravitational potential wells of minihalos (Johnson and Bromm, 2007; Whalen et al., 2008; Milosavljević et al., 2009). This suggests that the black hole seed must have been formed at redshift $z \geq 15$ with a mass of $\approx 10^5$, or the black hole seed had a lower mass but a high rate of growth, or a combination of both. As we can note in Fig. 1.1.1, there are some pathways for the formation of very massive objects. We will give a brief summary of these scenarios in the next subsections.

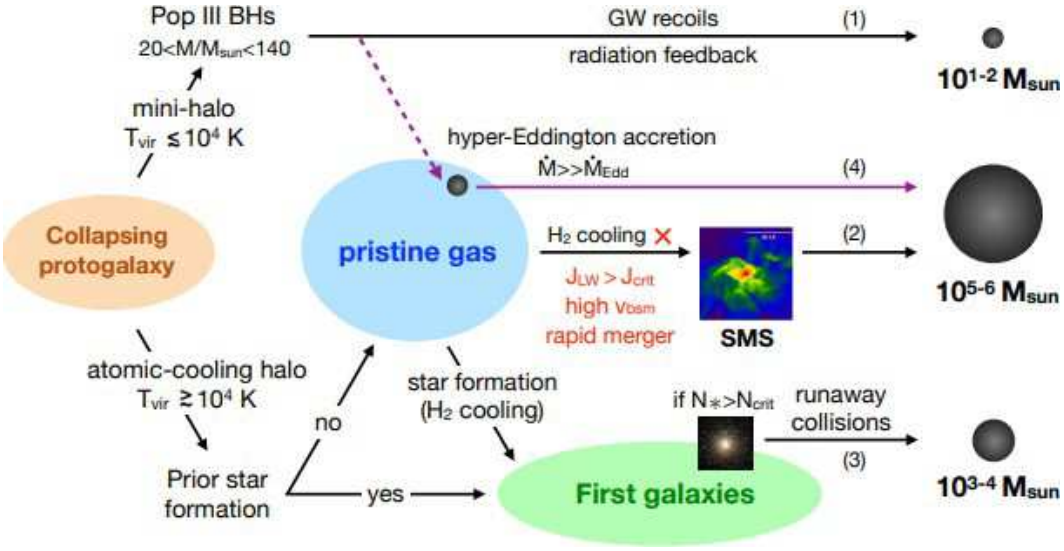

Figure 1.1.1: Different scenarios the formation of seed BHs on the top. 1) A BH remnant of a Pop III star with masses $\approx 10^{1-2} M_{\odot}$. 2) Massive seed BHs forming under conditions such as strong radiation, rapid mergers halos and high baryon-DM streaming velocities, reaching masses of$\gtrsim 10^{5-6} M_{\odot}$, 3) Formation of less massive intermediate massive black holes$\approx M^{3-4} M_{\odot}$ via runaway collisions in ultra-dense star clusters, 4) Finally the Hyper-Eddington accretion onto stellar mass BHs (Inayoshi et al., 2020).

1.2 Direct collapse

Direct collapse is one of the most promising scenarios of quasar formation at high redshift $z > 6$. It implies the formation of a massive BH seed of $10^5 - 10^6\, M_{\odot}$ via the gravitational collapse of a cloud of primordial gas (Rees, 1984; Bromm and Loeb, 2003; Koushiappas et al., 2004; Begelman et al., 2006), also called a direct collapse black hole (DCBH). These models invoke the rapid collapse of a chemically pristine primordial gas in so-called "atomic cooling halos"(ACHs). For this scenario to work the gas should efficiently redistribute angular momentum and rapidly collapse avoiding fragmentation. The main idea in this process is to bring large inflows of gas in a short time to the center of the halo via a large mass accretion rate of $\geq 0.1\, M_{\odot}/\mathrm{yr}$ (Begelman, 2010; Hosokawa et al., 2013; Schleicher et al., 2013).

This high accretion rate could be reached via thermodynamical processes by keeping the gas warm, where the mass inflow rate of the collapsing gas, the inflow gas mass rates are proportional to the temperature as $\dot{M} \propto T^{3/2}$ (Bromm

and Loeb, 2003). This relation can be derived dividing the Jeans mass $M_J \approx 2 \times 10^4 M_\odot n_H^{-1/2} T^{3/2}$ by the time free-fall $(G\rho)^{-1/2}$ time of the gas as follows:

$$\dot{M} \approx \frac{M_J}{t_{ff}} \approx 4 \times 10^{-3} \mathrm{M_\odot yr^{-1}} T^{3/2}. \tag{1.2.1}$$

Therefore higher temperatures imply large mass inflows rates. Hence, the thermodynamical way to form DCBHs requires warm gas to reach the critical mass inflow rate to form these objects, thus the gas in the halos should not cool down to lower temperatures, otherwise fragmentation and star formation could occur instead. The primordial metal free gas could also be cooling by the H_2 rovibrational lines bringing the gas to low temperatures of ≈ 200 K and triggering star formation. However, if the H_2 is dissociated the metal-free gas could reach temperatures of $\approx 10^4$ K triggering isothermal collapse forming objects with masses of $> 10^7 \mathrm{M_\odot}$.

The suppression of molecular hydrogen requires the presence of a Lyman Werner (LW) (Omukai, 2001; Omukai et al., 2008; Shang et al., 2010; Latif et al., 2013), flux by UV soft photons in $\approx 11 - 15$ eV, these are the transitions between the ground and excited electronic states of H_2, roughly 10% og the excitef H_2 decays radiatively into the split state of two H atoms. But the requirements of a strong LW fluxes could be reached as hosting halo should form in the vicinity of a massive star forming galaxy (Dijkstra et al., 2008). Numerical simulations have shown that the photodissociation of H_2 requires a very strong background (Bromm and Loeb, 2003; Wise et al., 2008; Latif et al., 2013).

The traces of H_2 in the primordial gas can be formed via two reactions :

$$H + e^- = H^- + \gamma,$$

$$H + H^- = H_2 + e^-.$$

The formation of H_2 can be suppressed in two ways either; directly by dissociation of H_2 or indirectly via photo-detachment of H^-. In the direct way photons with enough energy (ie. $11.2 - 13.6$ eV) can be absorbed by the Lyman-Werner bands of H_2 and photo-dissociate it via the Solomon process, and indirectly through energetic photons above 0.76 eV. The reactions are then the following ;

$$H_2 + \gamma_{LW} = H + H,$$

$$H^- + \gamma_{0.76} = H + e^-.$$

The critical value J_{crit} of the LW intensity for suppressing the H_2 abundance follows from balancing the dissociation rate ($\propto J_{LW} \times n_H$) and the formation rate ($\propto n_H^2$), and therefore the suppression of H_2 depends on the density n_H. The intensity varies between $J_{crit} \approx (0.01 - 1)J_{21}$, where J_{21} is in units of 10^{-21}erg s^{-1} cm^{-2} Hz^{-1} sr^{-1} (Haiman et al., 2000; Machacek et al., 2001; O'Shea and Norman, 2008). The intensity varies depending on the halo mass and the redshift.

For the thermal evolution of the gas there is a tight dependence on the LW intensity, particularly if it is below or above the critical intensity J_{crit}. In Fig. 1.1.1 when $J < J_{crit}$ (dashed blue curve) the temperature shows a rapid drop caused by the cooling of self-shielded H_2. In this case, the temperature track also converges with the solid blue curve without LW radiation. In the rapid cooling phase the gas is expected to fragment into small clumps with $M_J \sim 10^3$ M$_\odot$ (Regan and Downes, 2018). For $J > J_{crit}$ (solid red curve) the temperature evolution is nearly isothermal with $T \approx 8000$ K reaching high densities ($\sim 10^{16}$cm^{-3}) without being affected by the H_2 cooling. In this scenario the fragmentation at least is suppressed (Regan and Downes, 2018). To form a massive objects of mass $\approx M^6$ M$_\odot$ requires that the gas remains at a high temperature during the collapse phase driving an atomic cooling processes (e.g. $Ly\alpha$ emission).

Black curves show the temperature evolution in a gas polluted by metals and dust with $Z/Z_\odot = 10^{-4} - 10^{-5}$, leading to a rapid drop in the temperature due the thermal emission, driving a rapid cooling phase and therefore the gas likely will be fragmenting into smalls clumps forming regular stars.

In summary the formation of a massive seed BH is the result of an isothermal collapse by gravitational unstable primordial gas at high temperatures avoiding the processes of cooling, then producing a high accretion rate onto the central object and avoiding the episodes of gas fragmentation.

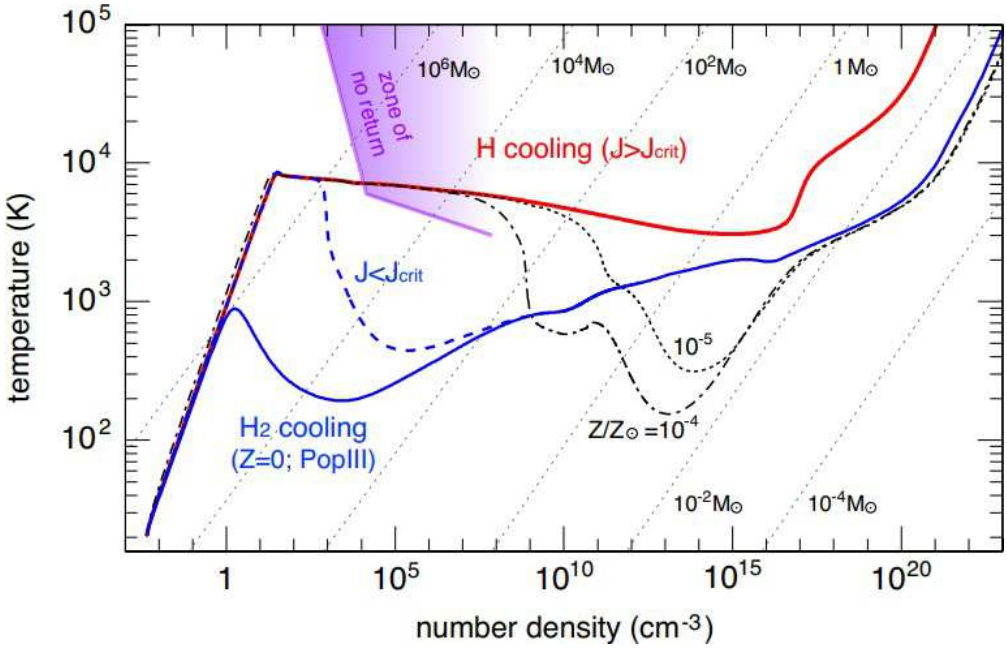

Figure 1.2.1: Temperature evolution of a metal-free gas cloud, irradiated by LW radiation. For high enough intensities ($J_{LW} > J_{crit}$) it is able to dissociate H_2 even in high density regions (red curves) (Inayoshi et al., 2020).

1.3 Formation of the first stars

The first generation of stars, the socalled population III (Pop III) generation, are formed at $z \approx 20 - 30$ in minihalos of $10^5 - 10^6 M_\odot$. The collapse of primordial gas clouds in these halos was triggered by the cooling processes of molecular hydrogen reducing the temperature to 200 K. The thermal Jeans mass scales with temperature $T^{3/2}$ so the mass scale of these stars is expected to be higher.

The protostars are born in a dense core embedded in a molecular hydrogen gas. The protostars grow either by mergers with other dense clumps or through gas accretion. In the first phase the star increases its radius during the adiabatic accretion $\approx 10^{-3} M_\odot/\mathrm{yr}$ reaching masses of $10 M_\odot$. Subsequently the star begins the Kevin Helmholtz phase (KH) radiating away its thermal energy. When the star begins to burn hydrogen and accretion stops, the star enters the zero age main sequence (ZAMS) with a mass around 100 $M_\odot$ (Omukai, 2001; Yoshida et al., 2006). The final mass of the star depends on the initial condition of the gas cloud such as its mass, spin, formation redshift and mass accretion rate (Hirano et al., 2014).

The UV feedback limits the stellar masses at lower accretion rates to at most a few $100 M_{\odot}$(Hirano et al., 2014). For mass inflow rates higher than $\gtrsim 0.1 M_{\odot}/\mathrm{yr}$, the envelope of the star is pulsationally unstable, to red giants and lost mass by this pulsations, similar due to the κ mechanism excited in the He^{+} ionization layer in the envelope (Inayoshi et al., 2013). However, the mass loss rate is negligible compared to the mass inflow rates, so the formation of a supermassive star (SMS) is not prevented neither by the UV feedback nor the pulsational instability.

The limit that a SMS could reach is given by a classical argument (Chandrasekhar, 1964); a SMS exceeding the critical mass M_{GR} collapses directly to a massive BH via the general relativistic (GR) instability. Haemmerlé (2020) found that critical mass is of the order $> 10^5\ M_{\odot}$. Shibata and Shapiro (2002) studied the gravitational collapse of rotating SMSs, and found that almost the complete stellar mass is swallowed by the new-born BH, ejecting only 10% of its mass. If the SMS is rotating sufficiently fast at the beginning of the gravitational collapse, the SMS collapses and a binary BH forms (Reisswig et al., 2013). Another proposed scenario is that only the central part of the SMS collapses forming a BH with mass $\sim 100 M_{\odot}$, and the envelope is inflated by the energy input from the gas that accreted onto the BH (Begelman et al., 2006).

1.4 Runaway collisions in a Dense Star Cluster

So far in the previous scenarios of massive seed BH formation, we talked about how the primordial gas undergoes gravitational collapse avoiding processes of cooling and fragmentation, but the issue that the cloud may fragment at very high densities is not entirely settled. The gas collapsing in the halo may have a modest level of pre-enrichment by metal/dust, so fragmentation could occur. The fragmentation opens another pathway to form massive seed BHs. The fragmentation at high density may give rise to the formation of an ultradense cluster (Omukai et al., 2008; Devecchi and Volonteri, 2009). Due to its high stellar densities ($\sim 10^{9-11} M_{\odot}/\mathrm{cm}^3$) this cluster can undergo runaway core collapse in a short time forming a central intermediate-mass black hole (IMBH) with mass of $\sim 10^{3-4}\ M_{\odot}$.

In this scenario a newly born dense star cluster could still be embedded in gas, which may help to form a massive BH seed by inflow of gas into the cluster (Tagawa et al., 2020), increasing its potential while decreasing the escapers and

deepening the potential well of the cluster. In this scenario the proto-star also could be accreting the gas increasing its radius hence its cross-section, and the gas dynamical friction driving a more efficient core collapse (e.g. Portegies Zwart et al., 2004; Reinoso et al., 2018).

In systems where massive black holes (BHs) form as a result of the dynamics in dense clusters, the contraction of these systems can be described with a negative heat capacity. The process can be described using a semi-analytic treatment of the energy transfer to the outer parts of the cluster (Lynden-Bell and Wood, 1968). In this bound system the negative heat capacity brings the core of the cluster in contact with the outer parts, it could act as a heat sink, thus it is possible that the core loses energy to the outer parts and contracts and heats up in the process, leading to core collapse or the "gravothermal instability".

In such a scenario at the moment of the core collapse, the core reaches such a high density that the collisions and mergers lead to the formation of a massive object. The binary heating in less massive star clusters may stop the core collapse (Heggie, 1975; Hut et al., 1992). On the other hand, mass segregation can lead to the formation of a massive BH seed even in less massive clusters (Heggie, 1975; Hut et al., 1992). Another way to form a massive seed black hole is via the merging of stellar mass black holes (Lupi et al., 2014) or a supra-exponential growth of stellar mass BHs in a cluster with dense gas (Alexander and Natarajan, 2014). Runaway merging may proceed in this regime because further BH mergers will be retained by the potential energy of the star cluster.

The relaxation time is related to the change and redistribution of the kinetic energy within the cluster by dynamical friction; this time scale is useful in understanding the evolution of the cluster, for a cluster consisting of stars with a single stellar mass it is given as

$$t_{rc} \approx \frac{0.065\, v^3}{nG^2 m^2 \ln\Lambda}, \tag{1.4.1}$$

where v is the rms velocity of the stars, m is the mass of one of the stars, n is the number density of stars, Λ is the ratio between the size of the system and the distance necessary for an encounter to deflect the star by $\pi/2$. For a cluster as a whole a useful concept is the relaxation time; this time scale changes relatively little through the evolution of some clusters, and describes the time necessary to

distribute the kinetic energy in the cluster by two body encounters. Considering virial equilibrium and equal mass stars the half mass relaxation is given by

$$t_{rh} = 0.138 \frac{N^{1/2} r_h^{3/2}}{m^{1/2} G^{1/2} ln\Lambda}. \tag{1.4.2}$$

Here N is the amount of particles in the cluster, r_h is the half mass radius of the cluster, the radius that contains the half mass of the cluster, the Coumlomb logarithm $\Lambda = \gamma N$, with $\gamma = 0.4$ (Spitzer, 1987).

A variation of this scenario consists of a less dense stellar cluster with more massive stars, with a rapid evolution collapsing and producing remnant stellar-mass BHs, which are embedded in a dense gas cloud. The mergers via dynamical friction and aided by gravitational waves (GW) could form a massive IMBH (Kroupa et al., 2020; Davies et al., 2011).

Chapter 2

Dark cores in nuclear star cluster

2.1 Model

The theoretical framework of this project is a variation of the model introduced in the previus section on runaway mergers in a dense star clusters. The model considers mergers in dense black hole clusters, following the framework of Davies et al. (2011). Due to mass segregation, the stellar mass BHs are assumed to have sunken to the center of the core of a nuclear star cluster. In stellar systems there is a the tendency toward equipartition of kinetics energies, so the most massive objects will tend to move more slowly on average and then massive object drops deep into the potential well, and light objects tend to move fast and move out, and may reach the velocity necessary to escape. This instability is known as the equipartition instability or Spitzer instability causing mass segregation, leading to the formation of a dark core. We assume that the stars and other remnants in the core of the cluster can be ignored as their individual masses are much smaller than those of the stellar mass BHs and thus they will be absorbed by the BHs or they may be pushed outside of the radius of the dark core (Banerjee and Kroupa, 2011; Breen and Heggie, 2013).The cluster which is more than $50\mathrm{Myr}$ old is assumed to consist of N equal stellar mass BHs, each with mass m_{BH}. Some BH - BH interactions can lead to escapers but a significant fraction of the initial stellar mass BHs remains in the cluster (Mackey et al., 2007)

Binaries within the dark core stabilise the cluster against core collapse as the binaries are a heating source (Hills, 1975; Heggie, 1975; Miller and Hamilton,

2002). Thus the dark core evolves as the BH population self-depletes through the dynamical formation of BH binaries in triple encounters which, after their formation, exchange energy with a third BH, where some interactions could lead to BH escapers, though due the deep potential well the cluster retains most of its BHs. According to the Hénon principle (Hénon, 1961, 1975), the energy generation rate in the cluster core from encounters between single BHs/binaries with hard binaries is regulated by the mass of the system. Such encounters transform binding energy into kinetic energy, which supports the cluster against core collapse. While soft binaries will be split by interactions in binary-single encounters, hard binaries tend to harden in binary-single encounters. We introduce here the critical value of the semi-major axis describing the transition between soft and hard binary systems,

$$a_{h/s} = \frac{Gm_1m_2}{< m > \sigma^2}, \tag{2.1.1}$$

where m_1 and m_2 are the masses of the primary and secondary of the binary system, $< m >$ describes the average mass in the cluster core and σ the velocity dispersion. Binaries with a semi-major axes $a > a_{h/s}$ are then referred to as a soft binary and will be disrupted due gravitational encounters, while only hard binaries with $a < a_{h/s}$ can survive. The timescale of a binary within a cluster to gravitational interact with another object is given by Binney and Tremaine (2008)

$$\tau_{2+1} \simeq 6 \times 10^8 x \frac{M_{c,6}^2}{v_{\infty,10}^3} \text{ yr}, \tag{2.1.2}$$

where $M_{c,6}$ is the total mass of the cluster in units of $10^6 M_\odot$, x is the ratio of binary binding energy to kinetic energy. In virial equilibrium we can consider that $v_{\infty,10} \approx 4.36\sqrt{GM_c/r_h}$ (Binney and Tremaine, 2008), where $v_{\infty,10}$ is the relative velocity at infinity in units of 10 km/s and r_h is the cluster half mass radius. Once the dark core reaches the critical density and a high enough velocity dispersion, the dynamical binaries formed in the cluster will be sufficiently tight to merge via gravitational wave (GW) emission, since the time scale of GW emission will be equal or shorter than the time scale of gravitational binary-single encounters. As the binding energy stored in the binaries is lost via GW emission, the binaries cease to be the source of heating of the cluster and core collapse takes place. The

decay time of a BH binary with an initial separation a and eccentricity e is (Peters, 1964)

$$\tau_{gw} \simeq 5 \times 10^{-3} c^5 G \frac{m_{bh}}{v_{\infty,10}^8} x^{-4} (1-e)^{7/2} \quad \text{yr}. \tag{2.1.3}$$

The gravitational binary-single interactions will leave the binaries with a thermal distribution of the orbital eccentricities, where the median eccentricity is $e_{med} = 1/\sqrt{2}$. This effect reduces the typical binary merger time by a factor of ≈ 10. Soft black hole binaries do not lose the necessary energy via gravitational radiation to merge, but if $\tau_{gr} < \tau_{2+1}$ binaries will merge avoiding the transfer of its binding energy to kinetic energy via gravitational interactions of the field, lose the energy that is stored in the binaries and thus the binaries will not keep heating the cluster as a result. Then the energy equilibrium breaks and core collapse is expected to happen. As we can note in Fig. 2.1.1, the solid dark line is the time scale of the inspiral time considering the real value of $c = 3 \times 10^5$ km/s and the dashed light green line is a cluster with mass $\approx 10^6 M_\odot$, so the core collapse could start when the velocity dispersion in the cluster reaches $\tau_{gr} < \tau_{2+1}$.

During the BH-BH mergers gravitational waves carry away linear momentum from the radiating source. This recoil is independent of the total mass of the system. When the BHs have the same masses gravitational beaming is symmetric and the recoil vanishes. Calculations which include gravitational redshift suggest that recoil velocities are much less than 500 km/s, so much higher than the velocity dispersion of a globular cluster of $\approx$ 30 km/s, but in a BHs cluster core with $v_\infty >$ 1000 km/s probably less than 80% of BHs will be retained in the cluster despite the gravitational recoil.

This scenario thus requires a mechanism to shrink the radius of the cluster and/or increase its mass. The dark core thus needs to become more dense, so that the black holes may merge via run-away processes and stay within the cluster. In the scenario proposed by Mayer et al. (2010), the self-gravitating gas is subject to instabilities that funnel much of the low angular momentum gas to the center to scales of 0.2 pc or less. It is thus very efficient in contracting the core of the cluster, to increase the central densities and enhance the mass segregation, leading to fast interactions between stellar mass black holes that could lead to a quick coalescence and the formation of a massive BH seed. High resolution cosmological

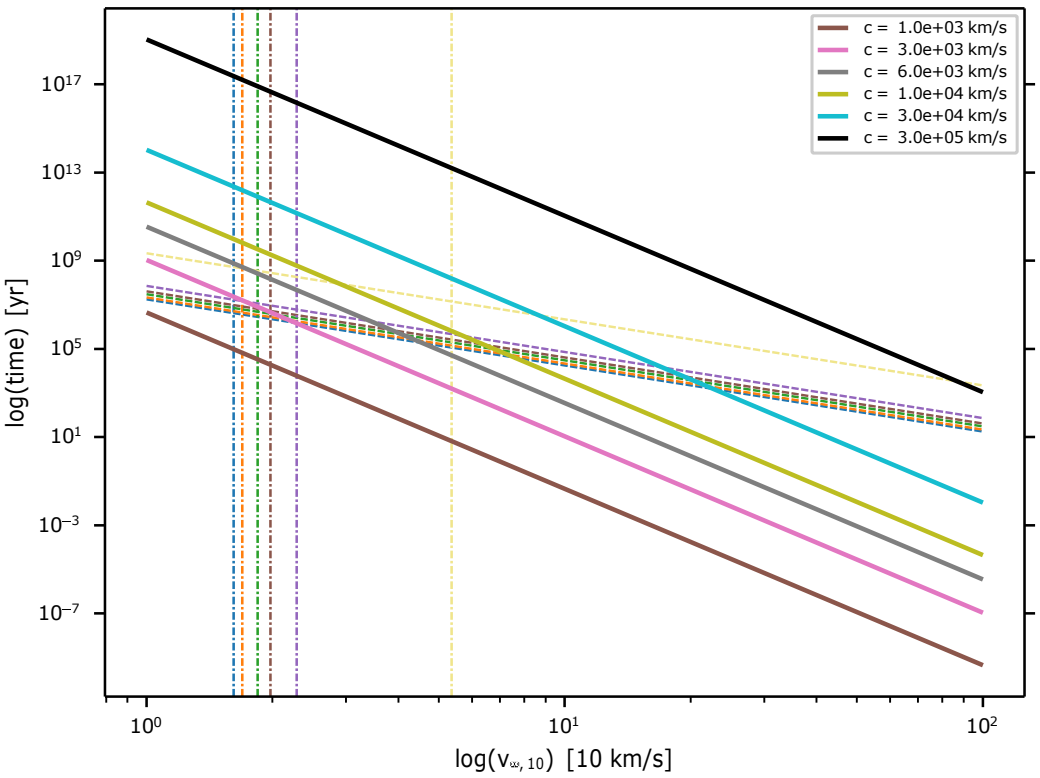

Figure 2.1.1: Logarithm of different time scales in years, the time scale for binary-single encounters give by eq. 2.1.2 (dashed line) and gravitational radiation inspiral given by eq. 2.1.3 (solid line), considering a variation on the gas mass fraction between $\eta_g = 0.0, 0.1, 0.3, 0.5, 1.010.0$, with the lowest value in the blue dashed line and the highest value light green line, considering different speeds of light, from $c = 10^3$ km/s to the real value of $c = 3 \cdot 10^5$ km/s (black line) and the lowest values of $c = 10^3$ km/s (brown line), the vertical lines show the velocity dispersion given by v_∞ for different gas mass fractions.

simulations of galaxy formation (Bellovary et al., 2011) show a gaseous inflow due to a combination of accretion of matter from the cosmic web-filaments and mergers of galaxies, providing a significant inflow of gas comparable to or higher than the stellar mass in the cluster at high redshift ($z > 10$).

Independent of the primordial mass segregation the inflow of gas into the cluster will make the black hole cluster shrink given the steeping of the potential. This increases the interactions between the BHs, while the initial fraction of hard binaries also affects the re-expansion of the cluster due to the heating of them. In this scenario the gas contributes only to deepening the potential well, while we neglect here the dynamical friction that could make the cluster even more dissipative and further enhance the probability to form a very massive object. Kroupa et al. (2020) have further investigated this scenario. They define the gas mass that falls into the black hole cluster $M_g = \eta_g N m_{BHs}$. They find this scenario to be feasible for $0.1 < \eta_g < 1.0$ with $R_{vir} \lesssim 1.5 - 4$ pc and $M_{BH} \gtrsim 10^4\, M_\odot$ where it could reach a relativistic state within much less than a Gyr , while for $\eta_g < 6$ the BH cluster expands because the binary heating dominates over the gas drag. For large values as $\eta_g > 6$ the black hole cluster may even be in the relativistic regime from the beginning.

The time scale for the cluster to undergo core collapse considering N equal mass BHs with a mass of m_{BH} is $t_{cc} \approx 0.15 t_{rc}$ (Gürkan and Rasio, 2005). t_{rc} is defined in Eq. 1.4.1. Considering the gas mass that falls into the cluster the half mass relaxation time is also affected. We consider a variation of the half mass relaxation time derived by Reinoso et al. (2020), which takes into a count the external potential,

$$t_{rh} = 0.138 \frac{N(1+\eta_g)^4}{ln(\gamma N)} t_{cross,ext}, \tag{2.1.4}$$

where η_g is the ratio of the gas mass fraction, $\gamma = 0.4$ for equal mass BHs, and the $t_{cross,ext} = t_{cross}/(1+\eta_g)$, where t_{cross} is the time necessary a BH to cross the cluster at rms velocity, $t_{cross} = R/V_{rms}$.

When the semi-mayor axis is sufficiently small, $t_{2+1} < t_{GW}$, and binaries merge before any other encounter happens. The inner part of the dark cluster has a high enough velocity dispersion σ so that $a_{h/s}$ can be sufficiently small for hard

binaries to merge via gravitational radiation. Such considerations give us a critical velocity dispersion of

$$\sigma_{crit} = \left(\frac{5}{64}\pi\rho_{BH} G^3 m_{BH}^2 c^5\right)^{1/11}, \tag{2.1.5}$$

where ρ_{BH} is the density of the dark cluster, m_{BH} is the mass of black holes, and c is it the light speed. When the cluster reaches the critical values in density (ρ_{BH}) and velocity dispersion (σ_{crit}) (Kroupa et al., 2020), the time necessary for the cluster undergo to the core collapse is given by

$$\frac{t_{cc}}{Myr} \approx 1.2 \times 10^8 \frac{1}{ln\Lambda} \left(\frac{m_{BH}}{M_\odot}\right)^{-5/11} \left(\frac{\rho_{BH}}{(M_\odot/pc^3)}\right)^{-8/11}. \tag{2.1.6}$$

Once σ reach the one percent of the light speed, the dark core is considered to be in a relativistic state (Kupi et al., 2006).

Chapter 3

Nbody6++GPU

To resolve the gravitational dynamics in the cluster, including post-Newtonian corrections, we use the Nbody6++GPU code (Wang et al., 2015). Nbody6++GPU uses a Hermite 4^{th} order integrator method (Makino, 1991). It also includes a set of routines to speed up the calculations such as using spatial and individual time steps and a spatial hierarchy which considers a list of neighbor particles inside a given radius, to distinguish between the regular force and the irregular force (Ahmad and Cohen, 1973). In this version the gravitational forces are computed by Graphics Processing Units (GPUs) (Wang et al., 2015). It further uses an algorithm to regulate close encounter (Kustaanheimo et al., 1965). Finally Nbody6++GPU includes post-Newtonian effects as described below (Kupi et al., 2006).

3.1 The Hermite integrator method

Each particle in our cluster is completely defined by its mass m, position $\mathbf{r}_0$ and velocity $\mathbf{v}_0$, where the subscript denotes the time zero t_0. The equation of motion for a particle i is given by its acceleration and his derivative $\dot{\mathbf{a}}_{0,i}$:

$$\mathbf{a}_{0,i} = -\sum_{j \neq i} Gm_j \frac{\mathbf{R}}{R^3}, \tag{3.1.1}$$

$$\dot{\mathbf{a}}_{0,i} = -\sum_{j \neq i} Gm_j \left[\frac{\mathbf{V}}{R^3} + \frac{3\mathbf{R}(\mathbf{V} \times \mathbf{R})}{R^5} \right], \tag{3.1.2}$$

where G is the gravitational constant, $\boldsymbol{R} = \boldsymbol{r}_{0,i} - \boldsymbol{r}_{0,j}$ is the relative coordinate and $\boldsymbol{V} = \boldsymbol{v}_{0,i} - \boldsymbol{v}_{0,j}$ the relative spatial velocity with respect to particle j.

The first approximation to the equation of motion of particles is a prediction via a Taylor series of the positions $\boldsymbol{r}_i(t)$ and the velocity $\boldsymbol{v}_i(t)$ for the next time step (t):

$$\boldsymbol{r}_{p,i} = \boldsymbol{r_0} + \boldsymbol{v}_0(t - t_0) + \boldsymbol{a}_{0,i}\frac{(t - t_0)^2}{2} + \dot{\boldsymbol{a}}_{0,i}\frac{(t - t_0)^3}{6}, \tag{3.1.3}$$

$$\boldsymbol{v}_{p,i} = \boldsymbol{v_0} + \boldsymbol{a}_0(t - t_0) + \dot{\boldsymbol{a}}_{0,i}\frac{(t - t_0)^2}{2}. \tag{3.1.4}$$

The predicted positions $\boldsymbol{r}_{p,i}$ and velocities $\boldsymbol{v}_{p,i}$, which result from this simple Taylor approximation, do not fulfill the requirements for an accurate high-order integrator. An improvement is made by a Hermite interpolation which approximates the higher accelerating terms by another Taylor series:

$$\boldsymbol{a}_i(t) = \boldsymbol{a}_{0,i} + \dot{\boldsymbol{a}}_{0,i} \times (t - t_0) + \frac{1}{2}\boldsymbol{a}^{(2)}_{0,i} \times (t - t_0)^2 + \frac{1}{6}\boldsymbol{a}^{(3)}_{0,i} \times (t - t_0)^3, \tag{3.1.5}$$

$$\dot{\boldsymbol{a}}_i(t) = \dot{\boldsymbol{a}}_{0,i} + \boldsymbol{a}^{(2)}_{0,i} \times (t - t_0) + \frac{1}{2}\boldsymbol{a}^{(3)}_{0,i} \times (t - t_0)^2. \tag{3.1.6}$$

Here the values of $\boldsymbol{a}_{0,i}$ and $\dot{\boldsymbol{a}}_{0,i}$ are known. To determine the higher derivatives of the accelerations terms we used the predicted $\boldsymbol{r}_p$ from Eq. 3.1.3 and $\boldsymbol{v}_p$ in Eq. 3.1.4; we calculate their derivative and call these new terms $\boldsymbol{a}_{p,i}$ and $\dot{\boldsymbol{a}}_{p,i}$, and replace r_p and v_p on the right hand of Eq. 3.1.5. And finally we have :

$$\boldsymbol{a}^{(3)}_{0,i} = 12\frac{\boldsymbol{a}_{0,i} - \boldsymbol{a}_{p,i}}{(t - t_0)^3} + 6\frac{\dot{\boldsymbol{a}}_{0,i} - \dot{\boldsymbol{a}}_{p,i}}{(t - t_0)^2}, \tag{3.1.7}$$

$$\boldsymbol{a}^{(2)}_{0,i} = -6\frac{\boldsymbol{a}_{0,i} + \boldsymbol{a}_{p,i}}{(t - t_0)^2} - 2\frac{2\dot{\boldsymbol{a}}_{0,i} + \dot{\boldsymbol{a}}_{p,i}}{t - t_0}. \tag{3.1.8}$$

Finally if we extend the Taylor series for $\boldsymbol{r}_i(t)$ and $\boldsymbol{v}_i(t)$ by two more orders and find the "corrected" positions and velocity to particle i at time t_1 as

$$\boldsymbol{r}_{1,i}(t) = \boldsymbol{r}_{p,i} + \boldsymbol{a}^{(2)}_{0,i}\frac{(t - t_0)^4}{24} + \boldsymbol{a}^{(3)}_{0,i}\frac{(t - t_0)^5}{120}, \tag{3.1.9}$$

$$\boldsymbol{v}_{1,i}(t) = \boldsymbol{v}_{p,i} + \boldsymbol{a}_{0,i}\frac{^{(2)}(t-t_0)^3}{6} + \boldsymbol{a}_{0,i}\frac{^{(3)}(t-t_0)^4}{24}. \tag{3.1.10}$$

The error in $\boldsymbol{r}$ and $\boldsymbol{v}$ within in two time steps $\Delta t = t1 - t_0$ is expected to be of order $O(\Delta t^5)$ and the global error for a fixed physical integration time scales with $O(\Delta t^4)$ (Makino, 1991). One of the advantages of the Hermite scheme is that it allows to use time steps twice as large for the same accuracy (Makino and Aarseth, 1992).

3.2 Individual and Block time steps

Stellar systems are characterized by a huge dynamical range in radial and temporal scales. The time scale varies e.g. in a star cluster from orbital periods of binaries of some days upto relaxation time scales of a few hundred millions year.

So in stellar systems we have a large dynamic range in the density from the center to the outskirts of the cluster, so those stars need to be treated different in the force calculation from the whole rest of the system. The objects that are in the outskirts of the cluster shall be allowed to move for longer distances before a re-computation of the gravitational force becomes necessary. This is the idea of a method for assigning different time-steps $\Delta t = t_1 - t_0$, in the force computation, the so-called "individual time-steps scheme" (Aarseth and Hoyle, 1963).

Given their high amount of elements, stellar systems are complex in their dynamical interactions over space and time scales,including binary systems with a period of only a few days to relaxation times of millions of years. Considering this range of time scales it is useful to use different time steps. Aarseth and Hoyle (1963) developed the ”individual time step scheme”, where the idea is to use small time steps to integrate particles in regions where the changes of the force are high, like for stars in the core of a star cluster, and large time steps for particles in regions of slowly changing dynamical force, like stars in the out-skirts of a star cluster, where they are allowed to move a larger distance before recomputing.

Each particle is assigned its own Δt_i as shown in Fig 3.2.1. This scheme is called "block time-steps". The particle i has the smallest time step at the beginning, so its phase space coordinate is determined at each time step. On the other hand, we have the particle k which has a time step twice as larger as the particle i, and

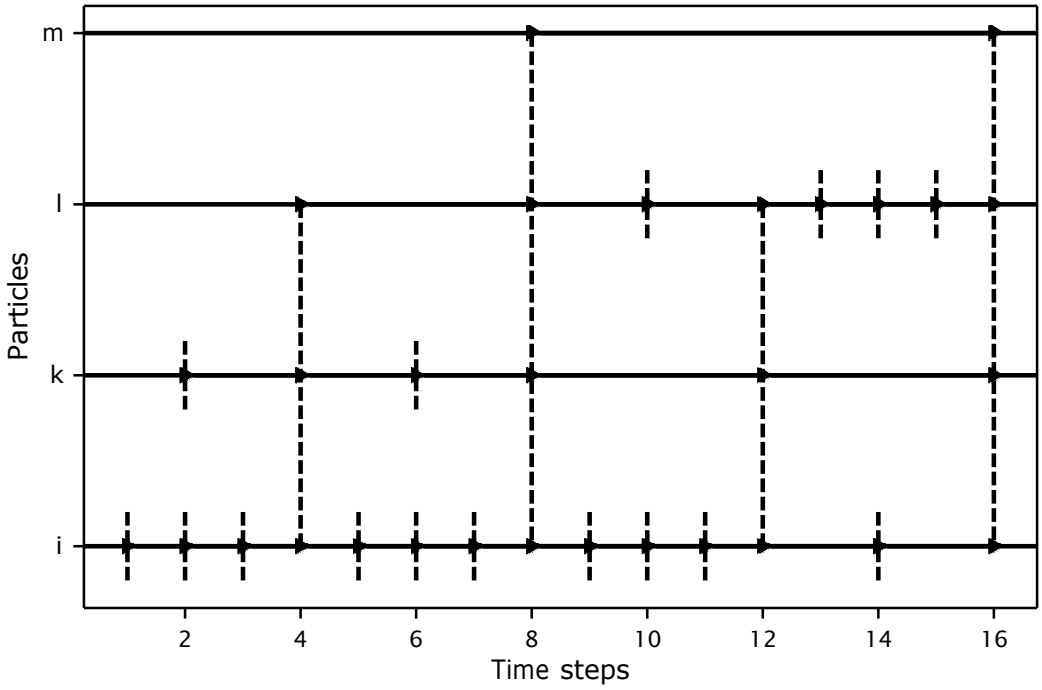

Figure 3.2.1: Regular and irregular time steps (Khalisi and Spurzem, 2014).

its coordinates are just extrapolated ("predicted") at the odd time steps, while a full force calculation is due at the black dots. Meanwhile the time steps in the simulation could change or not change during the evolution as we see for the particle k in figure 3.2.1.

A first approximation of the time-step comes from the rate of change in the acceleration $\delta t_i \propto \sqrt{a_i \dot{a}_i}$. A more accurate estimate in case of many-bodies is given by Aarseth (1985) avoiding some numerical error

$$\Delta t_i = \sqrt{\eta \frac{|\boldsymbol{a}_{1,i}||\boldsymbol{a}^{(2)}_{1,i}| + |\dot{\boldsymbol{a}}_{1,i}|^2}{|\dot{\boldsymbol{a}}_{1,i}||\boldsymbol{a}^{(3)}_{1,i}| + |\dot{\boldsymbol{a}}^{(2)}_{1,i}|^2}}, \tag{3.2.1}$$

where η is a dimensionless accuracy parameter which controls the error. In most applications it is taken to be $\eta \approx 0.01$ to 0.02. In the block-time steps, the synchronization is made by taking the next-lowest integer of Δt_i.

3.3 The Ahmad-Cohen scheme

The computation of the gravitational interactions between particles makes simulations very time-consuming for large numbers of particles, where the equations of motions to compute in the simulation scale with N^2 so at large N the time consumption increases rapidly. One method to speed up the calculations while retaining the collisions approach is by employing a "neighbour scheme" (Ahmad and Cohen, 1973).

The idea is to split the force polynomial 3.1.5 on a given particle i into two parts, an irregular and regular component,

$$\mathbf{a}_i = \mathbf{a}_{i,irr} + \mathbf{a}_{i,reg}, \tag{3.3.1}$$

where the irregular acceleration $a_{i,irr}$ results from particles in a certain neighbourhood of i (see Fig 3.3.1). The particles inside the neighbourhood give rise to a stronger fluctuating gravitational force, so it is calculated more frequently than the regular one of the more distant particles that do not change their relative distance to i so quickly. One can replace the full summation in Eq. 3.1.1 by a sum over the N_{nb} nearest particles for $\mathbf{a}_{i,irr}$ and add a distant contribution from all the others $\mathbf{a}_{i,reg}$.

To consider a particle inside the list of irregular particles it is necessary that particles are inside the "neighbor sphere" with radius r_s. In addition,we consider particles within a surrounding shell to satisfy $\mathbf{R} \times \mathbf{V} < 0$. This condition serves to identify particles that are rapidly approaching i.

The process of force calculation begins with a list of neighbours around the particle i shown as filled dots (see Fig. 3.3.1). From this list the irregular component $\mathbf{a}_{i,irr}$ due to the neighbours is calculated, and then the summation is continued to the distant particles, the regular component $\mathbf{a}_{i,reg}$. The time derivatives of two components are computed from equation Eq. 3.1.5 and 3.1.6, so the positions and velocities are predicted. At time $t_{1,irr}$ we only correct the $a_{i,reg}$ inside the neighbours, the regular component is not affected by the corrections. For the next time step $t_{2,irr}$ the same process is repeated. The distant particles are still unaffected by the acceleration corrections. When t_1 is reached we calculate the

total force on the basis of the full application of the Hermite predictor-method, and a new list of neighbours is constructed. With this scheme Nbody6++GPU in the irregular time only computes the forces of particles inside the neighbour radius, meanwhile in the regular time it computes all forces from neighbours and distant particles.

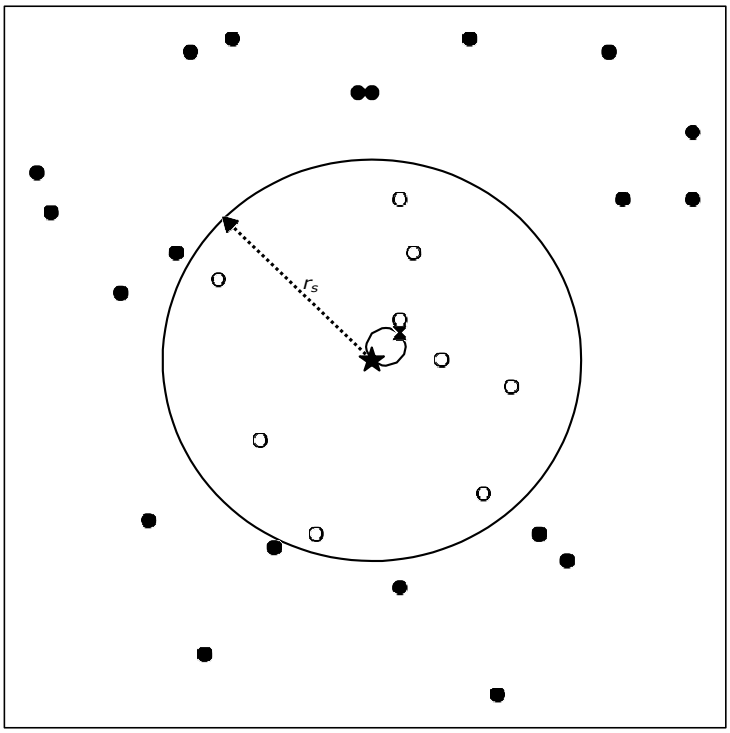

Figure 3.3.1: Illustration of the neighbour scheme. Particle *i* marked with an asterisk and the r_s neighbour radius. Black dots are particles that correspond to irregular forces and unfilled dots. Particles that correspond to the regular forces are marked as *X* to represent a close encounter (Khalisi and Spurzem, 2014).

3.4 KS Regularization

Close encounters of stars such as close binary systems or hyperbolic encounters need a special treatment. Their small distances and strong gravitational interactions lead to small time steps, making the particle integration computationally expensive. The main idea of the KS regularization implemented by Mikkola and Aarseth (1998), when two particles are as close as "X" in Fig. 3.3.1 with distances of hundreds of AU, is to take both close stars and move then out of the main integrator, replacing the system by their center of mass coordinate and go on with

the normal integration without both particles. The two close bodies are moved to another coordinate system and integrated separately from the rest of the particles, as the harmonic oscillator accurately describes the close encounter of two bodies.

The parameters involved in the regularization are **RMIN** and **DTMIN**, which refer to the minimum distance between two particles and their minimum time step, respectively, to be a considered as a regularized particle. They also need to fulfil 2 more criteria :

$$\mathbf{R} \times \mathbf{V} > 0.1 \sqrt{G(m_1 + m_2)\mathbf{R}}.$$

If the particles are approaching each other the value of 0.1 allows for nearly circular orbits to be regularized. The second criterion is

$$\gamma := \frac{|a_{pert}| \times R^2}{G(m_1 + m_2)} < 0.25,$$

so the relative force between the 2 particles is less than a quarter of the rest of the particles.

3.5 Post-Newtonian corrections

The relativistic stellar dynamics in stellar systems such as NSCs could give us a better understanding of the formation of SMBH, how massive central BHs could form from a given initial conditions, or to estimate the capture of compact objects on a central SMBH via extremely mass ratio inspiraling, etc. As we saw above Nbody6++GPU includes KS regularization, and this algorithm starts to operate when 2 particles are tightly bound. To avoid problems with small individual time steps, they are moved to another coordinates system. This scheme is modified to allow for relativistic corrections to the Newtonian forces by expanding the accelerations in a series of powers of $1/c$ (Soffel, 1989):

$$\underline{a} = \underbrace{\underline{a}_0}_{Newt.} + \underbrace{c^{-2}\underline{a}_2}_{1PN} + \underbrace{c^{-4}\underline{a}_4}_{2PN} + \underbrace{c^{-5}\underline{a}_5}_{2.5\ PN} + O(c^{-6}), \tag{3.5.1}$$

where $\underline{a}$ is the acceleration of the particle 1, $\underline{a}_0 = -Gm_2n/r^2$ is the Newtonian

acceleration, and 1 PN , 2 PN and 2.5 PN are the Post-Newtonian corrections to the Newtonian acceleration, where 1PN and 2 PN are the pericenter shift and 2.5 PN is the quadruple gravitational radiation. The corrections are integrated into the KS regularization scheme as perturbations, similarly to what is done to account for passing stars influencing the KS pair.

Other versions of Nbody also include relativistic effects. Nbody5 only includes wave emission terms, hence it neglected the 1PN and 2PN terms. The computation of PN is also CPU-time consuming, as it is necessary to compute both the accelerations and the time derivative. In the version of Nbody6++GPU that we use, 1PN,2PN, 2.5PN corrections are implemented without any further approximations (Soffel, 1989).

Another important topic in the relativistic dynamics is the gravitational recoil, the expected loss of linear momentum in an asymmetric system in which the remnant receives a kick from the gravitational waves emission. In the model used in Nbody6++gpu the series (eq. 3.5.1) is truncated at O^{-5} (Kupi et al., 2006), so the gravitational recoil is not consider in Nbody6++GPU.

Finally the criterion for particle mergers is calculated from their Scharzschild radii as

$$|R_{i,j}| \leq 2 \times \frac{G}{c^2}(m_i + m_j), \tag{3.5.2}$$

where G is the gravitational constant, c is the speed of light m_i and m_j the mass of particles i and j, with $|R_{i,j}|$ the distance between the particles in the binary system. This equation shows the minimal distance to consider a merge between two particles, and occurs when the distance between the particles is lower or equal of the sum of their Scharzschild radii.

3.6 Initialization of Nbody6++GPU

The input file that we use to model the clusters in this project is given as follows. We will also give a brief description of the template below.

```
1 1e6 1e6 40 40 0
N 10 10 NRAND 200 1 0 10
```

```
0.02  0.02  0.15  5.0  1.0  TCRIT  1.0E7  RBAR  ZMBAR
2  2  1  0  1  0  4  0  1  2
0  0  0  4  2  0  0  0  3  0
1  1  2  0  0  1  0  0  0  1
0  0  2  0  0  0  0  1  0  0
0  0  0  0  2  4  -6  0  0  1
DTMIN  RMIN  0.05  1.0  1.0E-06  0.01  0.125
1  100.0  CLIN  0  1.0
1.0  10.0  10.0  0  0  0.002  0.0  1.0
0.5  0.0  0.0  0.0
MP  AP  MPDOT  TDELAY
```

In the second row **N** is the number of particles in the cluster, **NRAND** is the seed to initialized the random position and velocities of each particle. In the third row **TCRIT** is the run time of the simulation in Myr, **RBAR** is the virial radius of the cluster in pc, **ZMBAR** is the mean mass of the particles in the cluster in solar masses, from row 4 to 8 are the KZ parameters which are explained in the manual of Nbody6++GPU (Khalisi and Spurzem, 2014). On row 9 we have **DTMIN** and **RMIN**, the parameters to define a close encounter between two particles. If two particles are closer than **RMIN** or have time steps lower than **DTMIN**, then they are candidates for regularization. The next row includes the parameter used for the Post Newtonian effects, the parameter **CLIN** is the speed of light in km/s. The last row is that used to define the analytic potential that we consider in the cluster; in our case it is a Plummer distribution settled with **KZ(14) = 4**, **MP** is the total mass of the Plummer sphere in Nbody-units, **AP** is the Plummer scale factor also in Nbody-units. Finally **MPDOT** and **TDELAY** are the decay time of the gas expulsion and the delay time for the gas expulsion, respectively.

3.7 Initial conditions

In this project we use the model introduced in Chap. 2 to explore the evolution and the formation of a SMBH seed in the dark core of a NSC. We perform a range of simulations to study how the presence of an external gas potential affects a dark core, the core collapse of the dark core and the growth of a SMBH seed

via run-away mergers. The configurations that we consider to model the dark core of a NSC is a spherical cluster of $N = 10^4$ stellar mass black holes with an identical mass of $M_{BH} = 10\ M_\odot$ at the beginning of the simulations. The spatial distribution is an isotropic Plummer sphere (Plummer, 1911) in virial equilibrium with virial radius of $R_v = 1.0$ pc. The analytic potential is given by a Plummer distribution with a mass $M_{gas} = \eta_g M_{Bhs}\ \mathrm{M}_\odot$ and a Plummer radius of $R_a = 0.56$ pc, where we vary the gas mass fraction of the cluster on $\eta_g = 0.0, 0.1, 0.3, 0.5, 1.0$.

The computations in such simulations considering the real value of the speed of light $c = 3 \times 10^5$ km/s become prohibitive. Here we try to extrapolate the behavior of the black hole cluster and the efficiency of formation of massive objects by taking c as a free parameter exploring the dependence on c and extrapolating to the real value of c. Mergers via gravitational radiation strongly dependence on the speed of light, as seen in Equation (2.1.3). When we increase the speed of light, the post-Newtonian effects become more prominent in the evolution of the cluster, and it takes more time to compute, eventually making it unfeasible to do computations for the real speed of light. Besides not only increasing the time for mergers, it also increases the time to solve the equation of motion, because as we see above in the Hermite scheme we need to compute not only the acceleration (see eq. 3.1.1) but also the derivative (see eq.3.1.2), and we need do this for every factor of the post-Newtonian corrections 1 PN,2 PN and 2.5 PN. Simulations considering the real speed of light could take months to model systems considered here. Therefore, we vary the speed of light in our simulations to study the dependence on post-Newtonian effects, with the goal of inferring what would occur in a dark core under realistic speed of light conditions. We vary the speed of light as $c = 10^3; 3 \times 10^3; 6 \times 10^3; 10^4, 3 \times 10^4$ km/s, and as a consequence it also affects the radii of the BHs in the cluster given by the Schwarzschild radii. The time evolution of all clusters is considered over a time of $T = 1.4$ Gyr. All configurations are given in table 3.7.1. For every setup we run 4 simulations, with different random initial conditions giving a total of 100 simulations.

Table 3.7.1: The initial amount of black holes in the cluster is N, the total mass in the cluster by BHs is M_{BHs}, the fraction of gas mass in the cluster is given by η_g, the virial radius R_v, finally the speed of light that we use in the simulation is given by c.

IDs	N	M_{BHs} [$M_\odot$]	η_g	R_v [pc]	c [km/s]
1	10^4	10^5	0.0	1.0	10^3
2	10^4	10^5	0.1	1.0	10^3
3	10^4	10^5	0.3	1.0	10^3
4	10^4	10^5	0.5	1.0	10^3
5	10^4	10^5	1.0	1.0	10^3
6	10^4	10^5	0.0	1.0	$3{\cdot}10^3$
7	10^4	10^5	0.1	1.0	$3{\cdot}10^3$
8	10^4	10^5	0.3	1.0	$3{\cdot}10^3$
9	10^4	10^5	0.5	1.0	$3{\cdot}10^3$
10	10^4	10^5	1.0	1.0	$3{\cdot}10^3$
11	10^4	10^5	0.0	1.0	$6{\cdot}10^3$
12	10^4	10^5	0.1	1.0	$6{\cdot}10^3$
13	10^4	10^5	0.3	1.0	$6{\cdot}10^3$
14	10^4	10^5	0.5	1.0	$6{\cdot}10^3$
15	10^4	10^5	1.0	1.0	$6{\cdot}10^3$
16	10^4	10^5	0.0	1.0	10^4
17	10^4	10^5	0.1	1.0	10^4
18	10^4	10^5	0.3	1.0	10^4
19	10^4	10^5	0.5	1.0	10^4
20	10^4	10^5	1.0	1.0	10^4
21	10^4	10^5	0.0	1.0	$3{\cdot}10^4$
22	10^4	10^5	0.1	1.0	$3{\cdot}10^4$
23	10^4	10^5	0.3	1.0	$3{\cdot}10^4$
24	10^4	10^5	0.5	1.0	$3{\cdot}10^4$
25	10^4	10^5	1.0	1.0	$3{\cdot}10^4$

Chapter 4

Results

In this section, we present the results of simulations in which we explore the behavior of the black hole cluster, taking into account the influence of an external potential, as well as variations in its potential mass. Additionally, we consider the effects of altering the speed of light in the context of Post-Newtonian effects and how these factors impact the evolution and growth of the central object. The setups we consider are detailed in Table 3.7.1. For each parameter listed in Table 3.7.1, we conducted four simulations with different random initial positions and velocities, resulting in a total of 100 simulations. In the next section, we will focus on four specific clusters with the following IDs: 1, 5, 21, and 25, as indicated in Table 3.7.1."

4.1 Dark Core Evolution

In Fig. 4.1.1, we illustrate the evolution of the dark cluster without an external potential (i.e., $\eta_g = 0.0$) while considering a speed of light of 10^3 km/s. The crossing time of the cluster, assuming no external potential, is calculated to be 0.0482 Myr. Additionally, the half-mass relaxation time as given by Eq. 2.1.4 is $166.38\, t_{cross}$. The cluster reaches its highest density at 85.194 Myr or, in terms of the half-mass relaxation time, at $10.61\, t_{rh}$. the inner parts of the cluster (10% Lagragian radii) reaches its highest density, measuring at 3.3×10^6 $M_\odot/pc^3$, with a 10% Lagrangian radius of 0.144 pc. In the first panel, we can observe that the 1% Lagrangian radius experiences a contraction and post-collapse oscillations. After the time of its highest density, the 5% Lagrangian radius shows a rebound,

and approximately 50 Myr later, it also experiences a contraction and begins to oscillate. A similar phenomenon occurs with the 10% Lagrangian radius, but with a longer delay in the collapse and subsequent oscillations. Lagrangian radii greater than 10% are affected by the expansion of the cluster.The second panel depicts the growth of the mass of the central object and the initiation of massive black hole formation. At time of highest density, the growth becomes exponential, occurring in a short span of approximately 10 Myr, eventually reaching a mass of 10770 $M_\odot$ by the end of the simulation. In the third panel, we can observe the escapers of black holes within the cluster and how they are influenced by prominent density at this point, resulting in a total mass loss of 21% within the cluster. The fourth panel illustrates the peak of mergers at the time when the cluster reach the highest density in the clusters, with approximately ≈ 80 mergers. There is a second peak occurring approximately ≈ 50 Myr later, with about ≈ 30 mergers, coinciding with the contraction of the 5% Lagrangian radius. we speculate that the event of shrink the Lagrangian radii of lower percents (< 10%) could be given by that the central object gain mass a high rate of mergers with other BH because this event math with the event of high rates of mergers.

In Fig. 4.1.2, we observe a cluster with η_g = 1.0 and a speed of light of 10^3 km/s. The crossing time is 0.0241Myr, and the half-mass relaxation time is $2662.149 t_{cross}$. The cluster experiences a high increase of the density at 450 Myr or, in terms of half-mass relaxation time, 7.010 t_{rh}. The density reached at the 10% Lagrangian radius is 1.23×10^6 $M_\odot/pc^3$, with a radius of 0.2 pc. The behavior of the cluster is remarkably similar to that of the cluster without an external potential. There is a delay in the contraction of higher Lagrangian radii after the collapse. The only difference is the duration of this delay, which is shorter, lasting only a few hundred Myr for the 10% Lagrangian radius. Additionally, post highest density in the inner reginons in the cluster, the cluster enters an oscillation stage affecting different percentages of the Lagrangian radii that have collapsed.

In the second panel, the mass of the central object exhibits a similar trend. The only difference is the occurrence of some mergers before this point of high density, and the final object is more massive, with almost twice the mass of the central object in the cluster without an external potential. In terms of escapers, this cluster experiences significantly lower mass loss compared to the cluster with η_g = 0.0, with a total mass loss of only 17% at the end of the simulation.

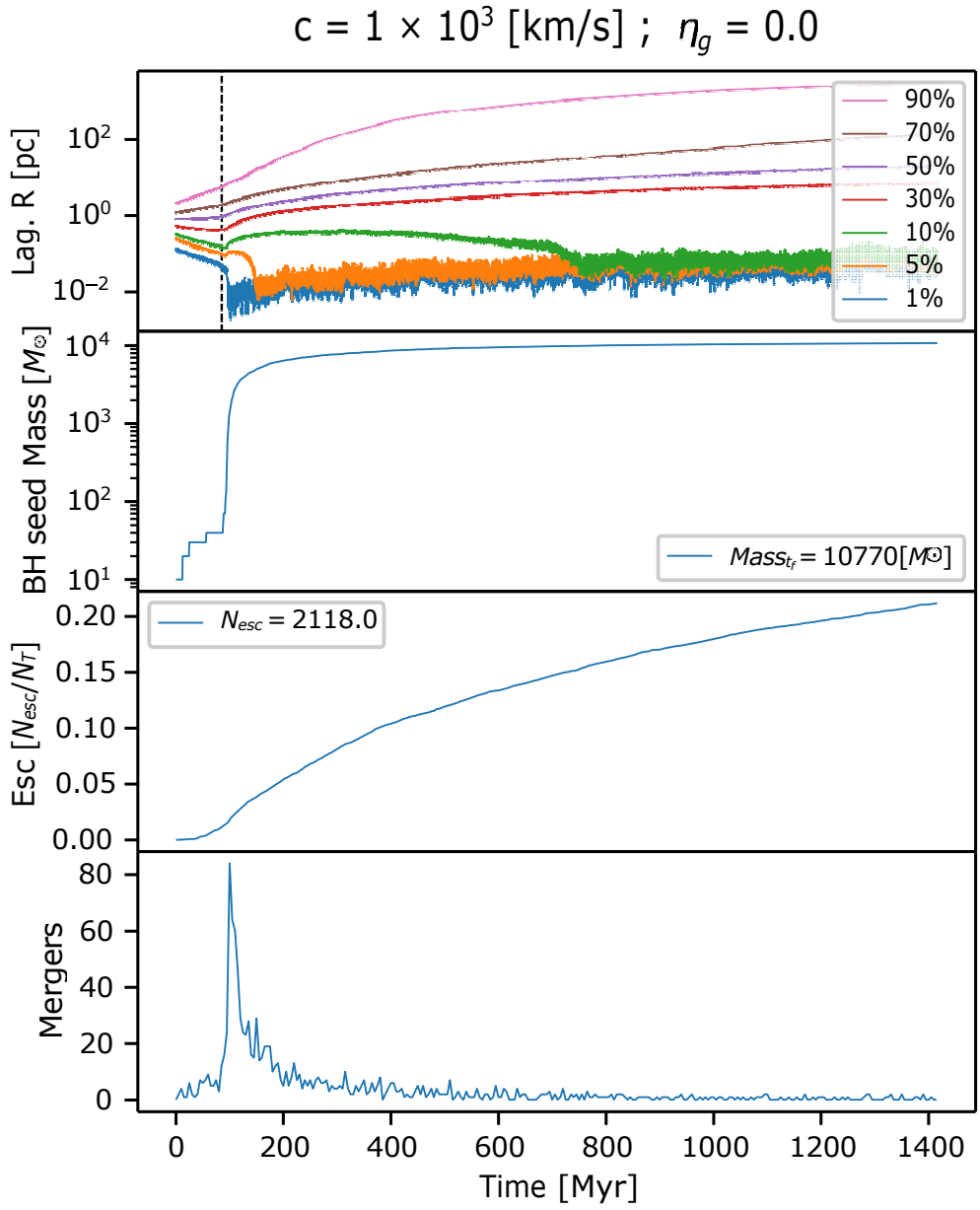

Figure 4.1.1: Evolution of the cluster in a simulation with speed of light c = 10^3 km/s without external potential. On the first top panel have the Lagrangian radius for mass fractions between 1% to 90% of the total cluster. The vertical line in this panel is the moment when the inner region reach the highest densities. The second panel shows the growth of the mass of the most massive BH in the cluster. The third panel shows the accumulative ejections in the cluster, and the lowest panel shows the mergers of BHs in bins of 5 Myr.

Finally, there are about 30 mergers at the time of a highst density in the inner regions. However, in contrast to the cluster without an external potential, the peak of mergers is shorter, and the mergers are more evenly distributed over time. Similar that the event in the cluster without external potential the shrinks of the Lagrangian radii of below 10% is also affected by the high rate mergers.

In Fig. 4.1.3, we depict the time evolution of a black cluster without an external potential while considering a higher speed of light of 3×10^4 km/s. The crossing time, based on the initial conditions of the cluster without an external potential, is 0.0482 Myr. Consequently, the half-mass relaxation time is calculated as $166.38\, t_{cross}$. The point of highest density occurs at $2268.70\, t_{cross}$, which translates to $13.63\, t_{rh}$ in terms of relaxation time. At the moment of highest density , the 10% Lagrangian radius reaches its minimum value of 8.4×10^{-2} pc, with a density of $1.65 \times 10^7\ M_\odot/\mathrm{pc}^3$. During the evolution of the cluster towards increase the density of the inner regions, we observe a contraction of the Lagrangian radii below 10%. Following this event, there is a slight expansion in both the inner and outer regions of the cluster. In the second panel, we illustrate the mass growth of the most massive object in the cluster, the SMBH seed. In a relatively short time range, this object gains a significant amount of its final mass, reaching a mass of $680\ M_\odot$ at 1.4 Gyr. Additionally, after the point of highest density, we observe a slight increase in escapers in the third panel, resulting in a total of 2473 escapers, accounting for almost 25% of the initial BHs in the cluster. In the fourth panel, we can see the BH mergers. The peak of the mergers is reached when the central regions contracts, with a peak of 15 mergers. Beyond the time of highest density, isolated mergers occur, with at most three mergers within 5 Myr

In Fig. 4.1.4, we explore a cluster with a comparable mass of the external potential and the BHs within the cluster, denoted as $\eta_g = 1.0$. The most notable distinction is the significant delay in the contraction of the inner regions compared to the clusters mentioned earlier. The highest density occurs at moment when the 10% Lagrangian radius reaches its minimum value, in this case, 8×10^{-2} pc with a corresponding density peak of $1.92 \times 10^7\ M_\odot/\mathrm{pc}^3$. This event occurs at 1137 Myr or, in terms of relaxation time, $17.77\ t_{rh}$. Before the highest density, only the Lagrangian radii lower than 10% experience contraction. After this event, unlike the clusters with a lower gas mass, the outer regions are less affected and do not experience significant expansion. Regarding the mass growth of the central object,

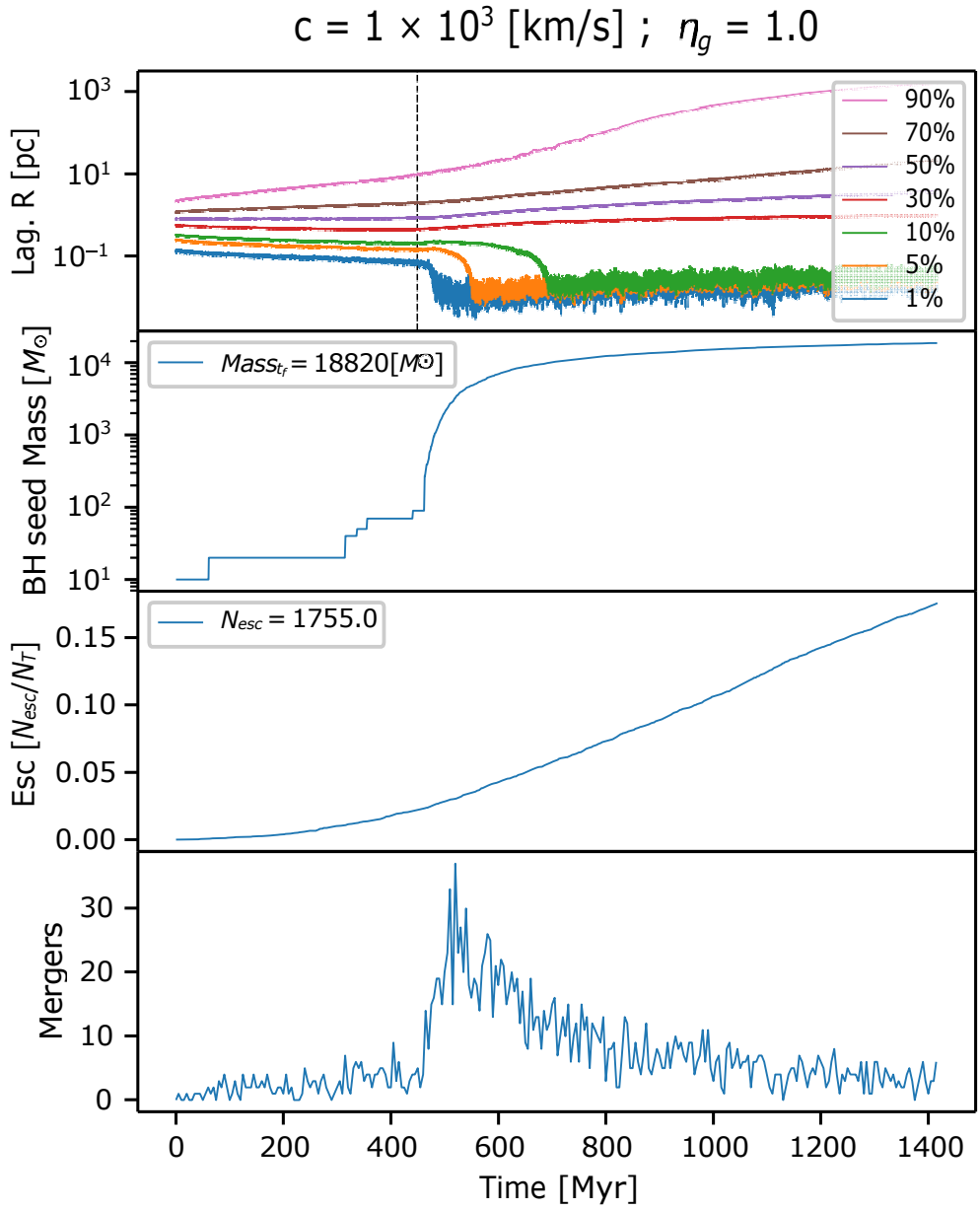

Figure 4.1.2: Evolution of the cluster in a simulation with speed of light c = 10^3 km/s and an external potential of η_g = 1.0. On the first top panel we show the Lagrangian radius for mass fractions between 1% to 90% of total cluster. The vertical line in this panel shows the moment when the inner region reach the highest densities. The second panel shows the growth of the mass of the most massive BH in the cluster. The third panel shows the accumulative ejections in the cluster, and the lowest panel shows the mergers of BHs in bins of 5 Myr.

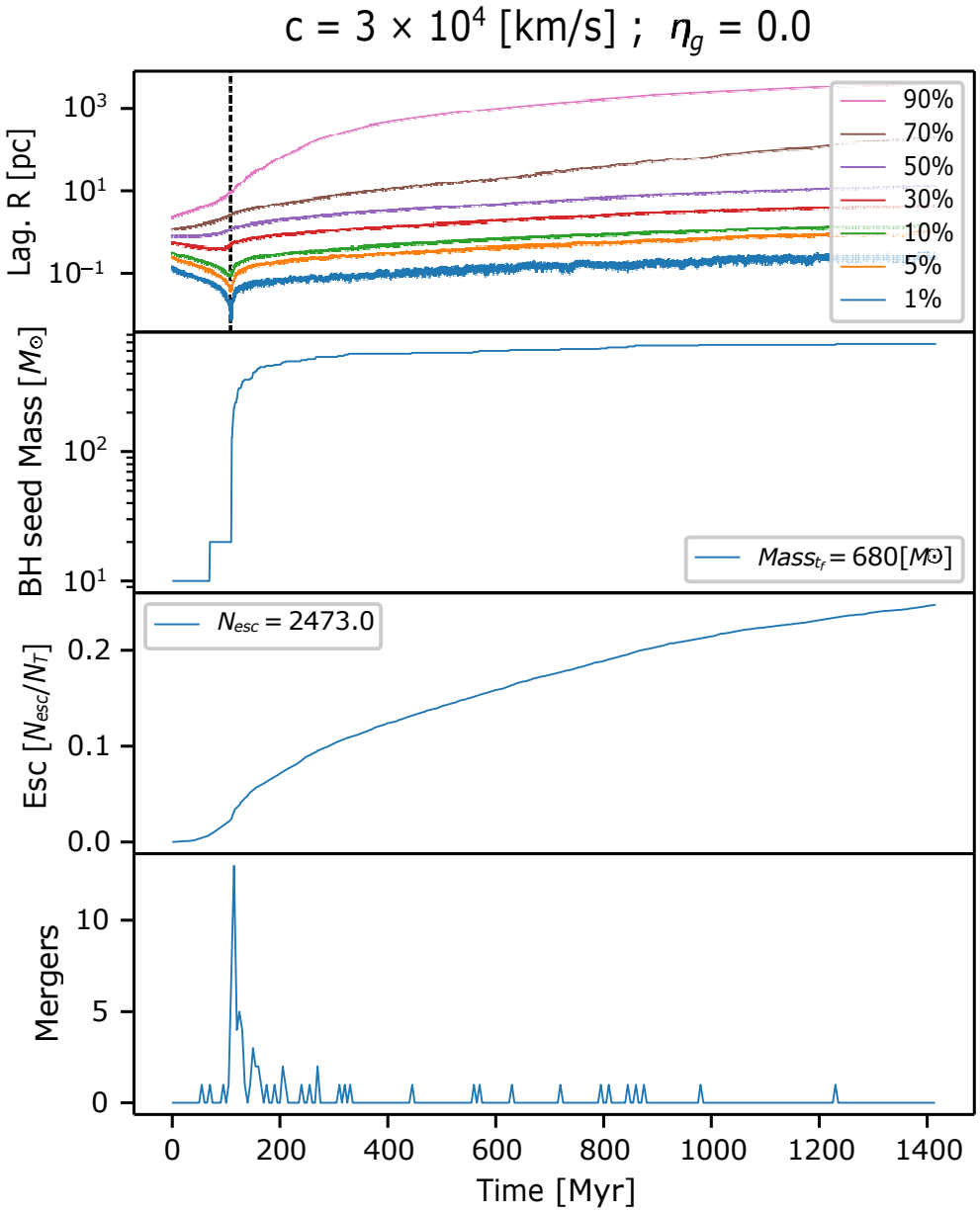

Figure 4.1.3: Evolution of the cluster in a simulation with speed of light $c = 3\times10^4$ km/s without external potential. On the first top panel we have the Lagrangian radius for mass fractions between 1% to 90% of total cluster. The vertical line in this panel is the moment when the inner region reach the highest densities. The second panel shows the of growth the mass of the most massive BH in the cluster. The third panel shows the accumulative ejections in the cluster, and the lowest panel shows the mergers of BHs in bins of 5 Myr.

it does not reach the same mass as in the other simulations, considering the gas mass fraction and the time required to reach at this point of contraction and high density. This discrepancy results from the time spent evolving the cluster after this event of high density. In terms of escapers, there is a slight bump at the of this contraction of the inner parts of the cluster. However, compared to the cluster without an external potential, this trend is steeper, resulting in a total of 1679 escapers, equivalent to 16% of the initial BHs in the cluster.

4.2 time dependence of core contraction

As we increase the external potential, one of the significant differences is the time it takes for the inner regions contraction to occur. As observed in the preceding sections, there is a difference of more than 1 Gyr between the cluster without a gas potential and the one with an equal mass fraction of gas and BHs, considering a speed of light of 3×10^4 km/s. However, at a lower speed of light of 10^3 km/s, there is a 450 Myr delay in time when occur that the inner region experience a contraction between the highest and lowest external potential. To estimate the of the core contraction time, we identify the peak of density at the 10% Lagrangian radius.

This even of highest density in the inner regions occurs between 6-20 half-mass relaxation times, as evident in Fig. 4.2.1. Assuming that core collapse is proportional to the relaxation time (Spitzer, 1987), we can infer that the time of contraction of the inner regions is proportional to $t_{cc} \propto (1 + \eta_g)^4 t_{cross}$, so the time of core contractions tends to be higher when the external potential increases (Reinoso et al., 2020). The linear trend suggests that clusters are more affected by gravitational radiation if the speed of light is reduced, thus making them more relativistic. We speculate this event of highest density event occurs even faster due to the emission of gravitational radiation. This is supported by the root mean square (rms) velocity in Fig. 4.2.2, which shows that the rms velocity is higher than 1% of the speed of light (10 km/s) that we consider in the simulation IDs 1-5, indicating that the BH cluster is in a relativistic state (Kupi et al., 2006). Furthermore, the relativistic state is more prolonged for higher external potentials, by the rms speed increases as the external potential increases, affecting the cluster via strong relativistic effects leading to the dissipation of

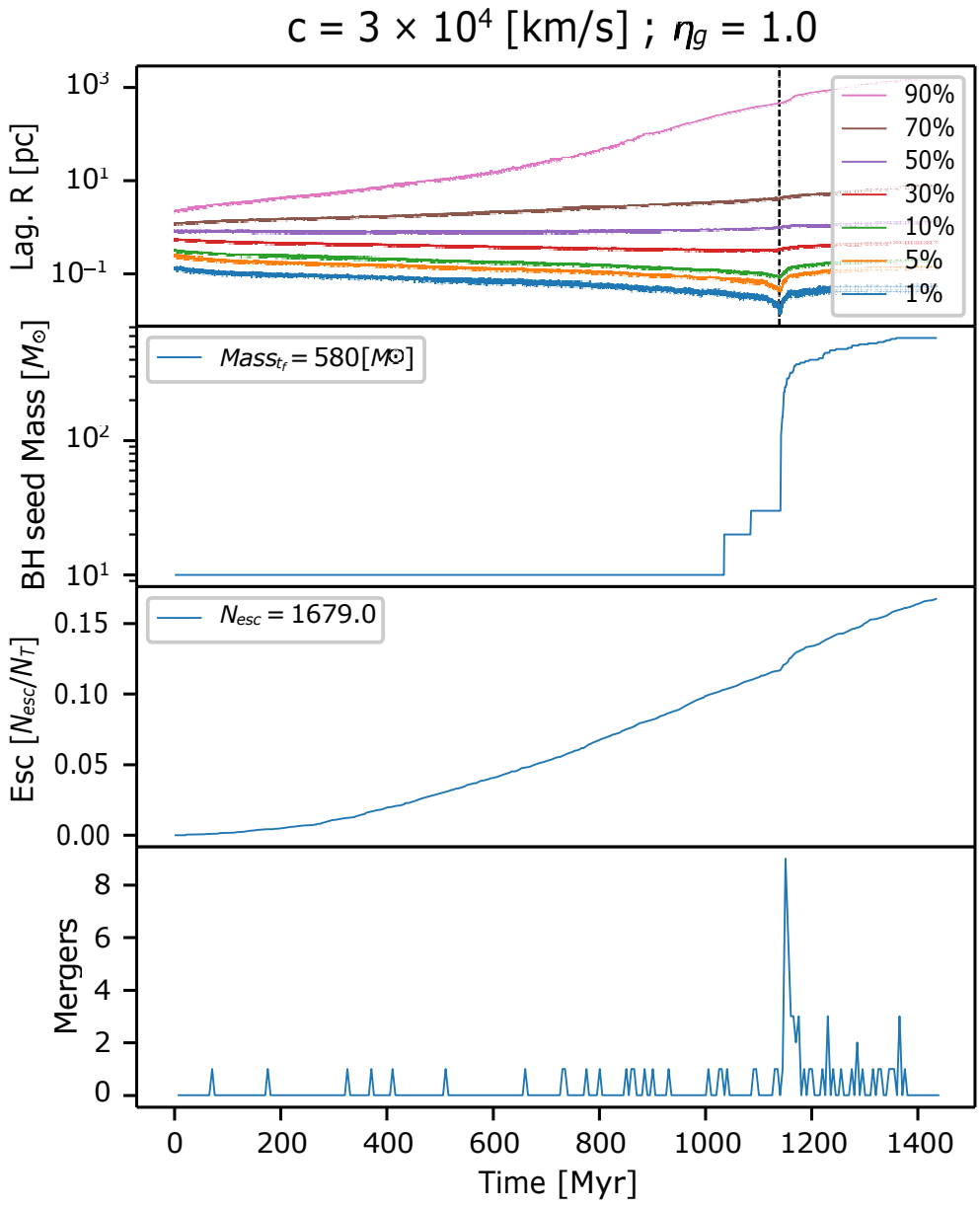

Figure 4.1.4: Evolution of the cluster in a simulation with speed of light c = $3 \cdot 10^4$ km/s and an external potential of η_g = 1.0. On the first top panel we have the Lagrangian radius for mass fractions between 1% to 90% of total cluster. The vertical line in this panel shows the moment when the inner region reach the highest densities. The second panel shows the of growth the mass of the most massive BH in the cluster. The third panel shows the accumulative ejections in the cluster, and the lowest panel shows the mergers of BHs in bins of 5 Myr.

kinetic energy into gravitational waves. For speeds of light exceeding 10^3 km/s, where $c = 3 \times 10^3$ km/s, we observe that the rms speed is slightly below 1% of the speed of light (30 km/s), but it is very close. Consequently, we might expect that gravitational radiation is not exceptionally strong, but it is still sufficient to reduce the time of highest density in the cluster, considering that the external potential increases the time of the event of high density. This is evident when examining the orange curve in Figure 4.2.1. However, for higher speeds of light, gravitational radiation is not strong enough, leading to a delay in the event of inner regions contractions.

In the right panel of Fig. 4.2.1, we observe the time of event of highest density as a function of the speed of light. It is evident that the external potential has a significant impact on the evolution of the cluster and time event of highest density, as reflected in the slopes of these trends. For clusters without external potential, there is almost no delay in the inner regions contraction of as the speed of light increases. In contrast, for clusters with an external potential of $\eta_g = 1.0$, the slope is much steeper. This results in a delay in the time of highest density of more than 700 Myr. This suggests that the time of highest density in clusters with a high fraction of gas mass is more affected. This impact can manifest as a decrease in the core contraction time due to gravitational radiation or an increase in the core contraction time due to dynamical friction, influenced by the added mass. The influence of the external potential on the time of highest density is particularly pronounced in clusters with a substantial gas mass fraction. This effect can lead to variations in the core contraction time time, making it an essential factor in the evolution of the cluster. For simulations with the different speed of light, we have calculated fits how t_{rh} depends on η_g, which we provide in the following:

$$\frac{t_{cc}}{t_{rh}}(\eta_g) = -3.728\eta_g + 10.449; \quad c = 10^3 \text{km/s},$$

$$\frac{t_{cc}}{t_{rh}}(\eta_g) = -0.043\eta_g + 11.991; \quad c = 3 \times 10^3 \text{km/s},$$

$$\frac{t_{cc}}{t_{rh}}(\eta_g) = 1.482\eta_g + 12.91; \quad c = 6 \times 10^3 \text{km/s},$$

$$\frac{t_{cc}}{t_{rh}}(\eta_g) = 3.32\eta_g + 12.874; \quad c = 10^4 \text{km/s},$$

$$\frac{t_{cc}}{t_{rh}}(\eta_g) = 5.631\eta_g + 12.681; \quad c = 3 \times 10^4 \text{km/s},$$

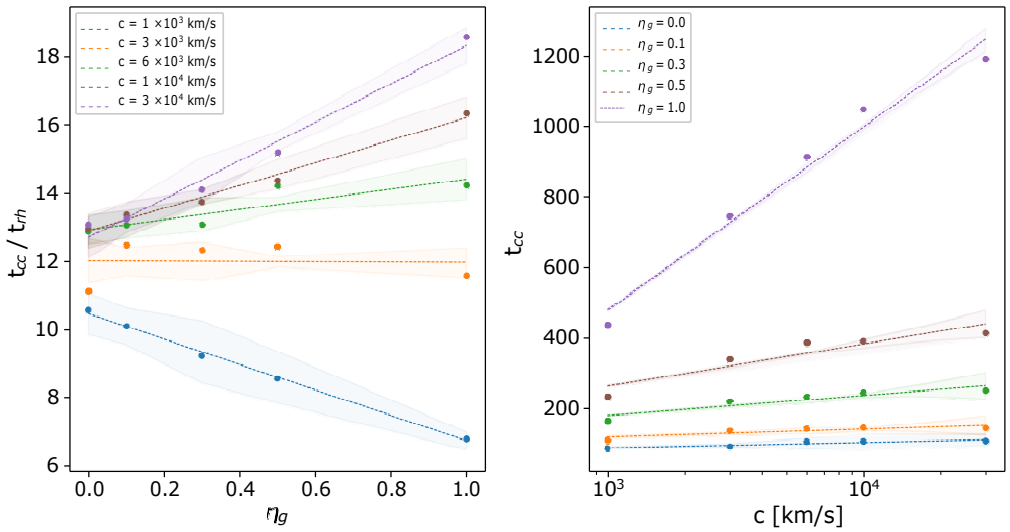

Figure 4.2.1: In the left panel, we depict the core collapse time relative to the half-mass relaxation time as a function of the gas mass fraction of the cluster, denoted as η_g. Each curve represents a different value of the speed of light, c. On the right panel, we illustrate the core collapse time relative time as a function of the speed of light, c. However, in this scenario, we vary the external potential, η_g. The shadow zone is the error computed by standard deviation with simulations at different initial conditions.

4.3 Binary population

Our simulations indicate that with respect to both the binary population and the mass of the cluster, the population of binary systems decreases when the cluster experiences a higher external potential. This trend is primarily attributed to the disruption of soft binaries resulting from the increase in the velocity dispersion within the cluster. In dense star clusters, binaries are influenced by two-body encounters, leading to their drift due to mass segregation. This is primarily because binaries possess a larger mass relative to single stars. In denser regions, the semi-major axis of binary systems tends to decrease over time, which leads to an increase in their hardness or their disruption via encounters with single stars.

In Fig. 4.3.1, we present a distribution of the semi-major axes of all binaries that are formed in the simulations, which demonstrates that binaries tend to

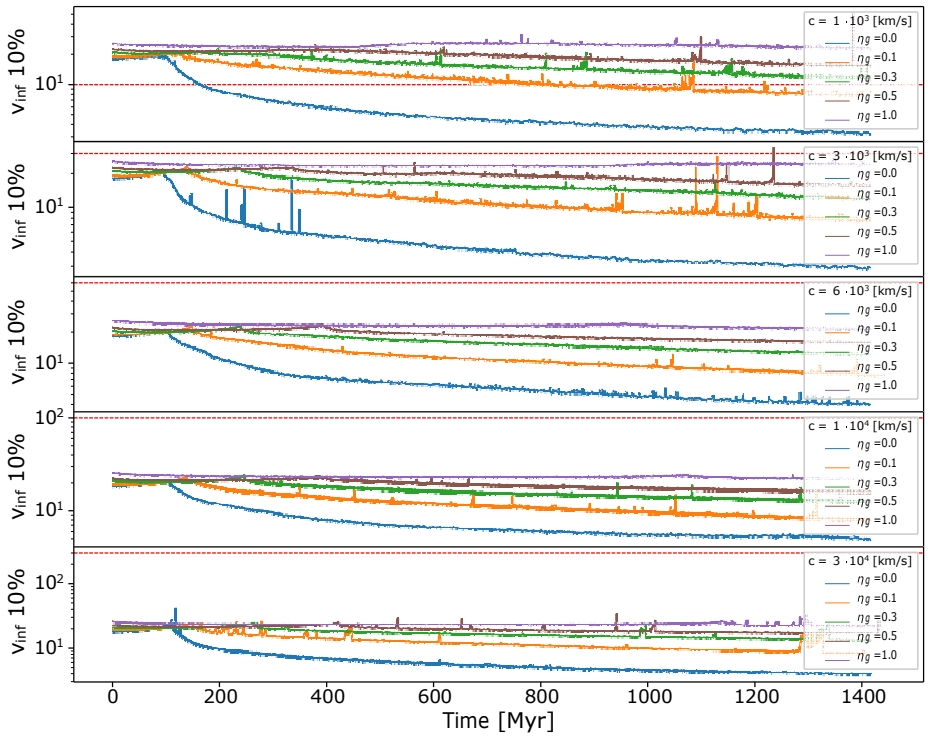

Figure 4.2.2: Evolution of the rms velocity over time, where the different panel correspond different speeds of light, on the top panel the lowest and to bottom panel the highest speed of light, for different external potentials (η_g). The horizontal red line correspond to the 1% of the light speed to check if the cluster could be in a relativistic state.

become more tightly bound when subjected to a stronger external potential. This phenomenon is particularly noticeable when they form at the hard-soft boundary, characterized by smaller values of the velocity dispersion, as outlined by Leigh et al. (2014). The ratio of hard/soft binaries appears to decrease as the external potential of the cluster becomes more massive. This can be explained by the Hills-Heggie law, which describes the semi-major axis at which the orbital energy equals the average kinetic energy of single stars (see Eq. 2.1.1). When the semi-major axis is smaller than a_{HS}, the binary is considered a hard binary and tends to have a higher binding energy following single encounters. This increases the likelihood of merging due to gravitational waves. Conversely, binaries with a larger semi-major axis than a_{HS} are categorized as soft binaries and are more likely to expand their semi-major axes before encounters, making them prone to ionization. This observed trend of an increasing ratio of hard to soft binaries with the rise in the external potential of the cluster is likely to have a significant impact on massive black hole growth. This impact is manifested in terms of binary mergers and cluster escapers, affecting the mass loss of the cluster through single-binary encounters.

To provide a clearer view of the trends in the semi-major axis at different external potentials, we calculated the standard deviation of the semi-major axis distribution mentioned previously. In Fig. 4.3.2, the left panel demonstrates an increase in the semi-major axis up to $\eta_g = 0.1$. As the external potential increases, it becomes evident that binaries tend to become more tightly bound, resulting in a significant reduction in the spread of the semi-major axis, nearly by one magnitude, when $\eta_g = 1.0$. On the other hand, in the right panel of Fig. 4.3.2, we have the semi-major axis dispersion as a function of the speed of light. We can observe that the semi-major axis remains almost flat for speeds of light lower than 10^4 km/s, and for higher values, it tends to decrease. This behavior may be attributed to hard binaries, which tend to persist because the inspiral time scale is longer, leading to a delayed merger of black holes. In contrast, soft binaries become less bound by dynamical friction and may even dissociate. As a result, the average dispersion of the semi-major axis tends to become less spread.

In Figure 4.3.3, we observe a distribution of eccentricities in binaries of all binaries that are formes in the simulations. We notice that the shape of the distribution remains relatively consistent across different external potentials. The binary

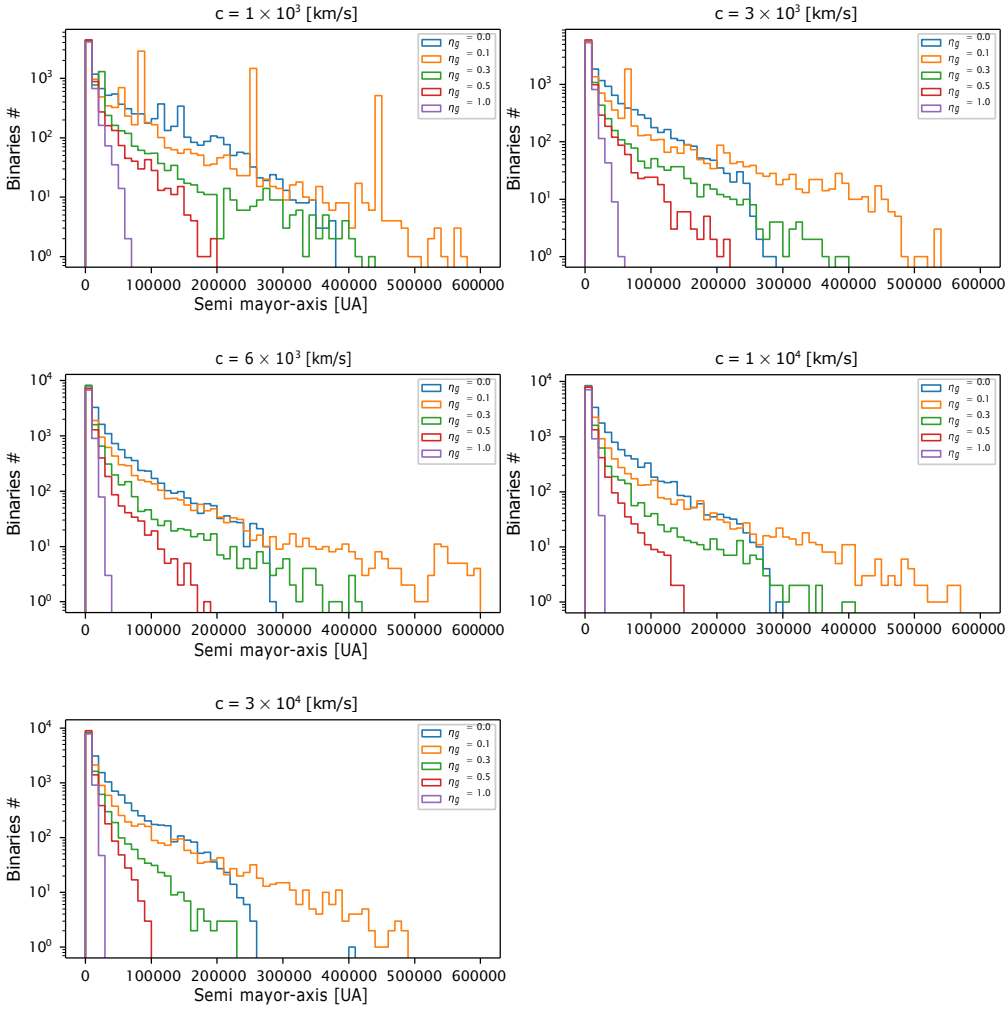

Figure 4.3.1: Distribution of the semi-mayor axis of binaries in the cluster for different values of c and η_g, of all binaries that formed in the simulations.

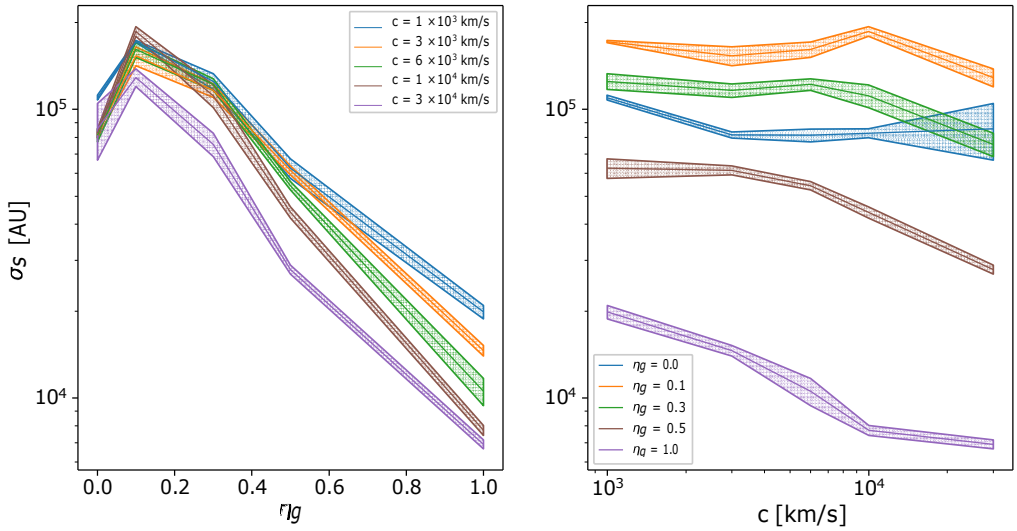

Figure 4.3.2: The standard deviation of the semi-major axis is derived from the distribution in Fig. 4.3.1. On the left panel, we observe the trend of the semi-major axis concerning the external potential. On the right panel, we depict the semi-major axis in relation to the speed of light.

eccentricity distribution exhibits a steep increase in eccentricities, reaching a peak at around 0.9, and then it decreases for binaries with higher eccentricities. The shape of the distribution is similar to all clusters, but the differences in the external potential lead to significant variations in the population of binaries. This is because the formation of binaries through three-body encounters is less frequent when the velocity dispersion is higher due to time scales of $t_{3bb} \propto M^3/\rho^{1/2}$.

We can also observe that the formation of binaries tends to result in high eccentricities. This may be due to the fact that these systems initially possess high eccentricities or evolve to such states through interactions. As a result, circular orbits are rare, either because these objects are dissociated, or they increase their eccentricities through gravitational interactions. The initial assumption of τ_{gw}, considering a thermal distribution with an eccentricity of $e_{med} = 1/\sqrt{2}$, appears to be a reasonable approximation. Additionally, it seems that e_{med} is independent of the external potential.

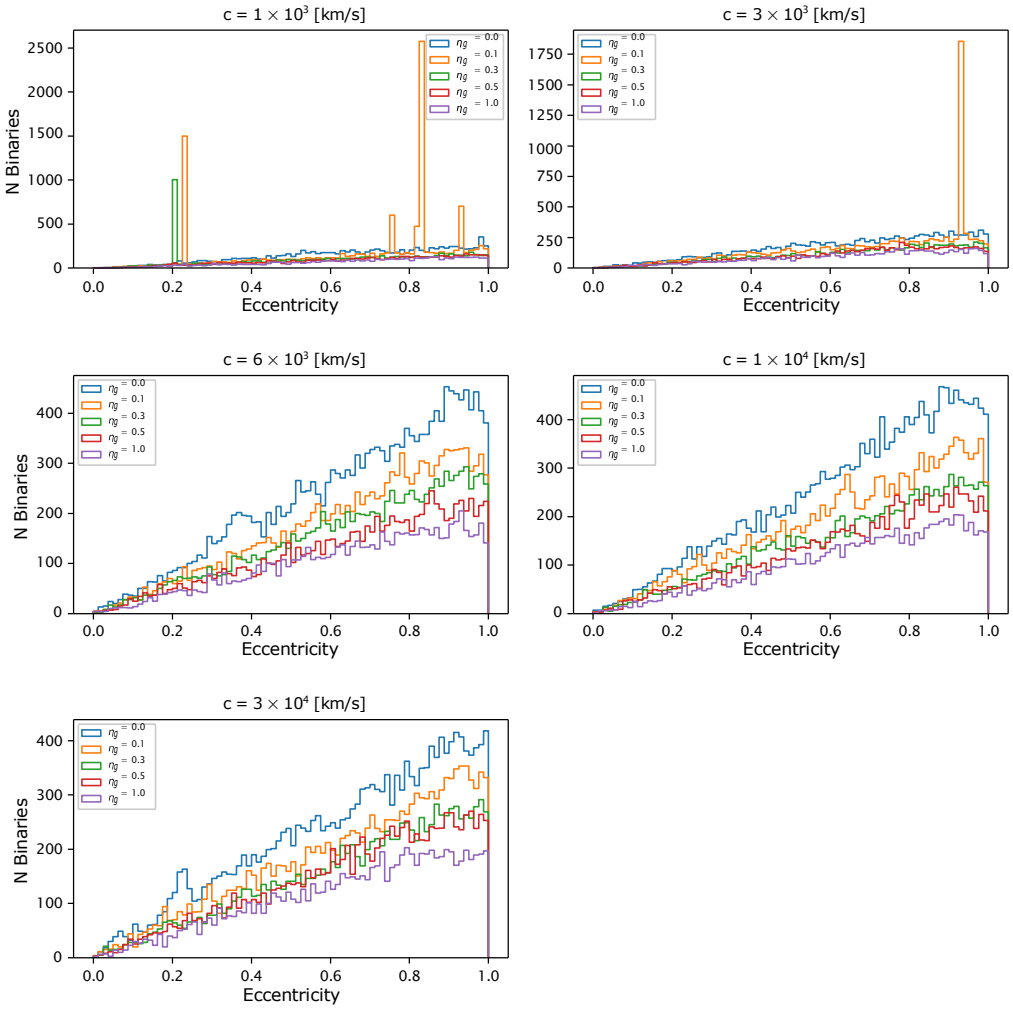

Figure 4.3.3: Histogram of binary eccentricities where the different panels correspond to different value of the speeds of light, and the colors show different external potentials (η_g).

4.4 Escapers

Escapers in star clusters can be triggered by three distinct mechanisms: a single encounter with another BH can produce a velocity change comparable with the initial velocities of the two BHs. The second mechanism involves a series of weaker, more distant encounters that gradually increases the energy of a BH. Eventually, after a last, weak encounter that imparts slightly positive energy, the BH escapes. We refer to this process as 'evaporation.' The third and final mechanism is related to the asymmetric emission of gravitational radiation. BH remnants receive a kick, providing the kinetic energy required to escape the cluster. The magnitude of this kick depends on the mass ratio and spins of the BHs. However, as mentioned earlier, this mechanism does not affect our simulations.

The escape velocity as a function of the cluster mass and density is given by (Georgiev et al., 2009)

$$v_{esc} = 40 \mathrm{kms}^{-1} \left(\frac{M_{NSC}}{10^5 M_\odot} \right)^{1/3} \left(\frac{\rho_{NSC}}{10^5 M_\odot \mathrm{pc}^3} \right) . \tag{4.4.1}$$

Equation 4.4.1 takes into account the mass and density of the NSC. However, it is important to consider that we might be overestimating the number of escapers from the dark core. We are, in essence, neglecting the mass outside the dark core, which could significantly increase the total mass of the cluster. The mass of the NSC can vary within the range of $10^5 - 10^9\ M_\odot$ (Georgiev et al., 2016). The loss of mass due to escapers plays a pivotal role in the evolution of the cluster and the formation of Intermediate-Mass Black Holes (IMBHs). The energy lost from the cluster due to the escape of BHs leads to a heating of the cluster, contributing to its overall dynamics.

In Fig 4.4.1, we observe the evolution of escapers in terms of crossing times. It is evident that all clusters exhibit a similar trend in the behavior of escapers at different values of the speed of light. The escapers are notably influenced by the core contraction and high densities in the inner regions of the cluster, with the highest density events reaching densities of approximately $10^6 - 10^7\ M_\odot \mathrm{pc}^{-3}$. This increase in density leads to a subsequent rise in the number of escapers, primarily due to both weak encounters (evaporations) and strong encounters resulting in ejections. The escapers generally follow a consistent pattern with occasional

fluctuations, possibly associated with oscillations in the inner regions that, in turn, impact the density.

On the other hand, there is a notable difference between clusters with varying external potential. Initially, the clusters without external potential exhibit a higher number of escapers compared to clusters with higher external potential. However, after a few thousand crossing times, clusters with $\eta_g = 0.1$ and $\eta_g = 0.3$ reach or even surpass the escaper count of the cluster with $\eta_g = 0.0$. This outcome might not align with our expectations, especially when considering higher-mass clusters as described in equation 4.4.1, but it could be related to the evolution of the binary population (see below). In the case of a higher external potential, such as $\eta_g = 1.0$, there is a substantial reduction in the number of escapers, with only a fraction of the cluster having escapers compared to clusters with lower external potential.

In Figure 4.4.2, the total number of escapers is compared after 29031 crossing times (given by the cluster with $\eta_g = 0.0$). On the left panel, the number of escapers in the cluster is plotted as a function of the external potential. We can observe that for $\eta_g = 0.1$, the number of escapers shows a small increase, independent of the speed of light. As the external potential increases ($\eta_g > 0.1$), the number of escapers starts to decrease with a steep slope, diminishing even more rapidly as η_g approaches 1.0. This trend appears similar to the trend of the semi-major axis of the binary systems (see Fig. 4.3.2). These trends could be connected, considering that the timescale for a binary-single encounter can be expressed as (Heggie and Hut, 2003):

$$t_{ce} = \frac{\sigma}{8\pi G \rho_{BH} a}, \tag{4.4.2}$$

where ρ_{BH} is the total mass density in the cluster and a is the semi-major axis of the BH binary, so t_{ce} becomes smaller for high a, as a result we could expect to have more weak encounters between binary-single BH providing the energy necessary to escape from the cluster. On the other hand, the right panel shows the number of escapers as a function of the speed of light. As we can note the slope is almost flat so the numbers of escaper do not change with the speed of light.

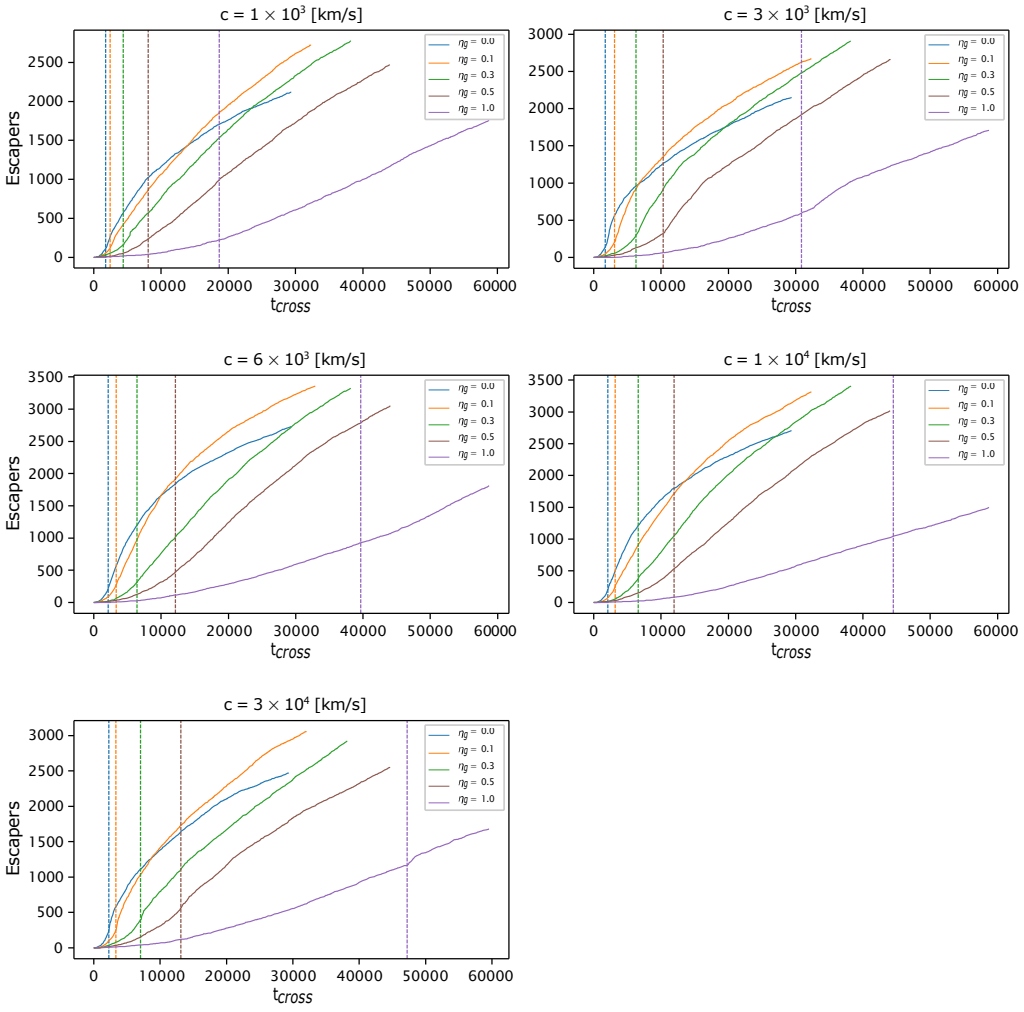

Figure 4.4.1: Accumulative numbers of escapers as a function of crossing times, considering different external potentials marked by their colors, and for different speeds of light. The vertical line marks the time of the core collapse.

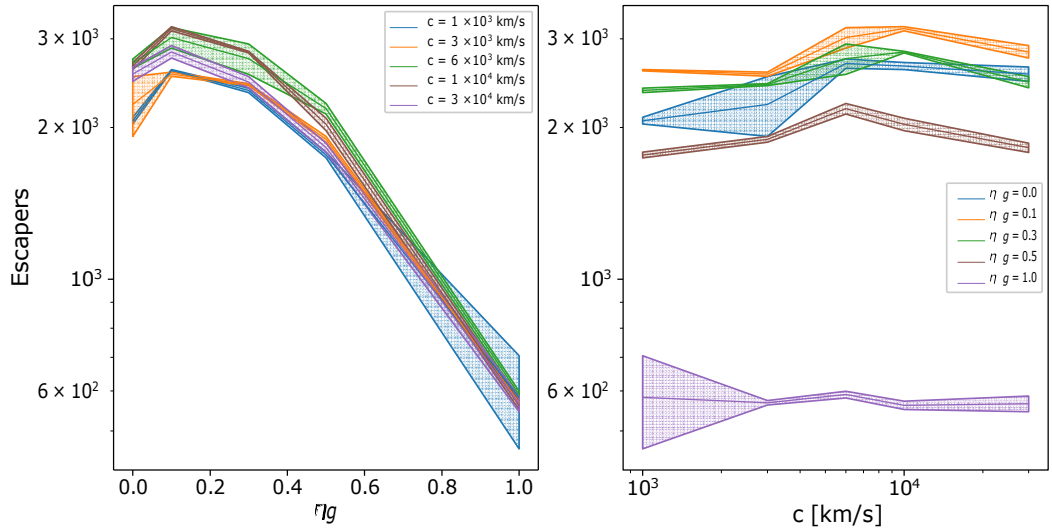

Figure 4.4.2: On the left panel we have the escapers as a function of the external potential. On the right panel the escapers are given as a function of the speed of light. In both panels shown the escapers at the same crossing of 29031 crossing times shown in the Fig. 4.4.1

4.5 Formation of IMBH

From all these results, we can observe that binary systems play a pivotal role in the evolution of star clusters and the formation of Intermediate-Massive Black Holes (IMBHs). From the moment of highest density on the inner regions to the generation of escapers and IMBH formation, binaries are central to these processes. Previously, we discussed how the formation of an IMBH can take place through mergers of stellar-mass black holes when the inspiral timescale for these mergers is shorter than the timescale for binary-single encounters. The conditions for this scenario are most favorable during core contraction when the cluster experiences high densities and velocity dispersion, allowing binaries to merge via gravitational radiation.

As we can observe in Figures 4.1.1 and 4.1.2, mergers of black holes can occur independently of the core contraction event. This indicates that the conditions for these mergers are not exclusively confined to the core contraction phase. Consequently, the timing of the highest density can provide more time for the central massive black hole to grow, especially in clusters with a low gas mass fraction, as depicted in Figure 4.2.1. Hence the massive black hole could enhance

the BH binaries mergers via Kozai-Lidov mechanism (Sedda, 2020; Aarseth, 2007), the process by which the large eccentricities are attained is due third-body secular perturbations.

Additionally, the external potential has a significant impact on the binary population by reducing the number of binaries available for mergers. This reduction binaries could affect in the mass of a central massive black hole. Moreover, the external potential also delays the timing of core contraction. However, it is important to note that the density and velocity dispersion within the cluster are essential factors for the formation of "hard" binaries, which are more likely to merge due to gravitational radiation.

In Figure 4.5.1, we observe the evolution of the most massive black holes (BHs) in the cluster over relaxation time scales. As mentioned earlier, core contraction and high densities leads to a high rate of mergers in a short period, resulting in the formation of objects as massive as 70 solar masses ($M_\odot$) before feeding the BH seed. This, in turn, leads to a rapid increase in the mass of the BH seed, a phenomenon observed in all clusters.

When comparing clusters with different external potentials, it is evident that higher external potentials result in the BH seed reaching a higher mass over the same relaxation time. However, this trend of higher external potentials leading to a more massive BH seed begins to decrease as the speed of light increases. In such cases, the clusters tend to have a smaller difference in the mass of the central object, as we saw before when increasing the speed of light the gravitational radiation is reduced increasing the time scale of mergers. Also the time of contraction of inner regions is delayed even more when the speed of light increases (see Fig. 4.2.1). In some instances, this clusters with low external potential even end the simulation with a more massive BH seed. This occurrence is attributed to having more relaxation times for to evolution after core contraction .

In Fig. 4.5.2 we have a plot that shows the dependence of the final mass of the BH seed on the external potential (top-left panel) or the speed of light (top-right panel). We provide fits of the BH mass as a function of the external potential considering different speeds of light in equations 4.5.1 - 4.5.5 with a linear fits of $M_{BH} = \beta\eta_g + \gamma$; we note that it is a linear trend for speeds of light $< 10^4$ km/s. The slope (β) of the trend increases so the mass of the BH seed becomes more

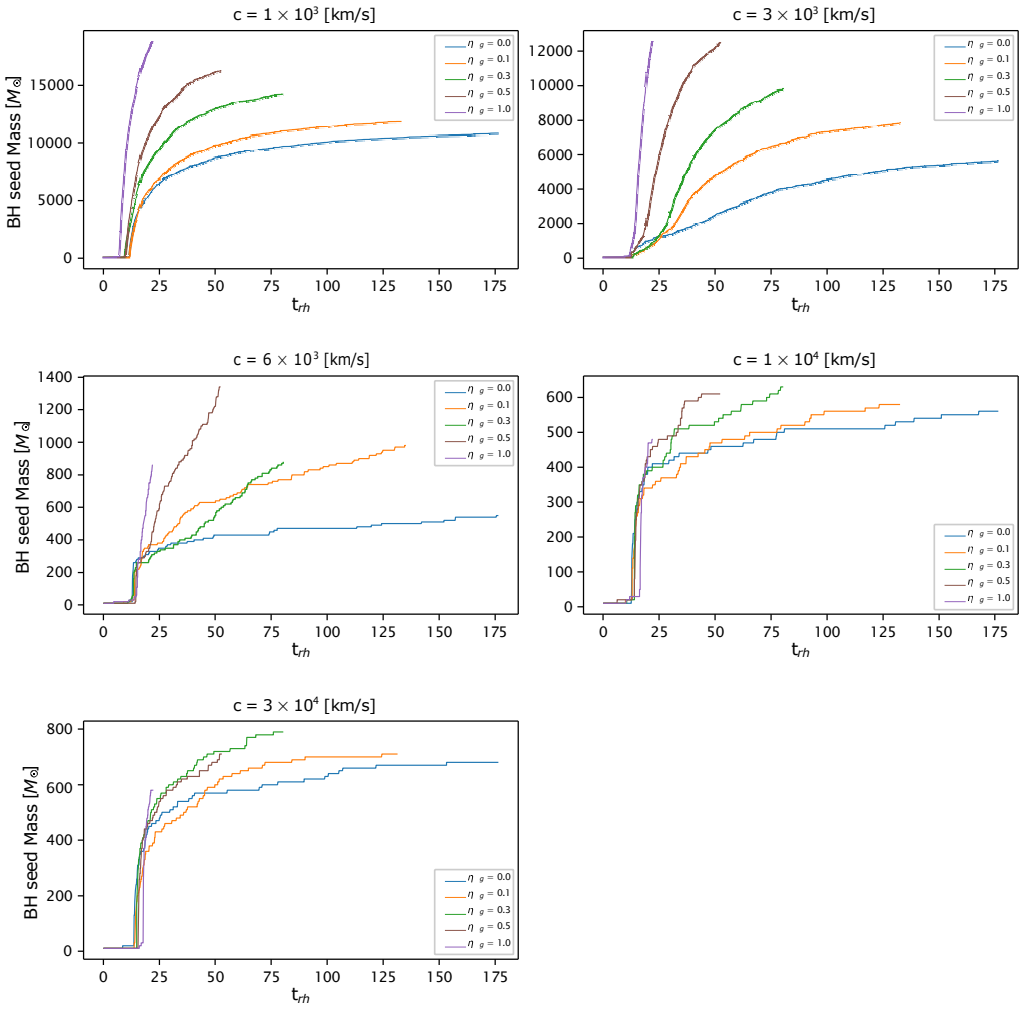

Figure 4.5.1: Mass growth of the most massive BH in the cluster over time in relaxation time scales, where the different colors mark the external potential of the cluster (η_g). Different panels shows the speed of light (c) considering in simulations.

massive for higher external potentials. On the another hand, for $c \geq 10^4$ km/s, the slope of the trend is negative so for higher external potentials the mass of BH seed tends to decrease. As we noted above this is due to the decrease of the available time as a result of the the delay of the core contraciton.

Also we can note how the second parameter (γ) increases considering relativistic clusters, independent of the external potential of the cluster, giving us 2 sets of BH seeds, the massive BH seeds with mass $\approx 10^{3-4} M_\odot$ for speeds of light $< 6 \times 10^3$ km/s , and the lower massive BH seeds of $\approx 10^2 M_\odot$ for speeds of lights $\geq 6 \times 10^3$ km/s. The dependence of η_g can be summarized as follows:

$$M_{BH}(\eta_g) = 7812.022\eta_g + 11448.431; \quad c = 10^3 \text{km/s}, \tag{4.5.1}$$

$$M_{BH}(\eta_g) = 5063.854\eta_g + 7331.736; \quad c = 3 \times 10^3 \text{km/s}, \tag{4.5.2}$$

$$M_{BH}(\eta_g) = 114.013\eta_g + 960.175; \quad c = 6 \times 10^3 \text{km/s}, \tag{4.5.3}$$

$$M_{BH}(\eta_g) = -22.85\eta_g + 617.683; \quad c = 10^4 \text{km/s}, \tag{4.5.4}$$

$$M_{BH}(\eta_g) = -156.529\eta_g + 738.981; \quad c = 3 \times 10^4 \text{km/s}. \tag{4.5.5}$$

On the right panel of Fig 4.5.2 (top-right panel), we show the mass of the BH seed at the end of the simulation as a function of the speed of light. The fits that we provide are described by equations 4.5.6-4.5.10. As mentioned earlier, the BH seed mass tends to increase for higher external potentials, except for clusters with speeds of light $> 6 \times 10^3$ km/s. The trend of massive BH seeds at speeds of light $< 6 \times 10^3$km/s, with masses of $\approx 10^{3-4}\ M_\odot$, transitioning to less massive BH seeds $\approx 10^2\ M_\odot$ at speeds $\geq 6 \times 10^3$km/s is evident.

For clusters with $\eta_g = 1.0$ and speed of light of 3×10^4 km/s, the BH seed mass becomes less than that of clusters with lower external potentials. This is primarily due to the time of core contraction, as clusters with lower external potentials have more time to evolve and then the BH seed grows in mass. We summarise here the dependence on c for different value of η_g:

$$M_{BH}(c) = 10199.391 \times \exp\left(-\frac{c}{3227.732}^4\right) + 624.143; \quad \eta_g = 0.0, \tag{4.5.6}$$

$$M_{BH}(c) = 10782.525 \times \exp\left(-\left(\frac{c}{3568.121}\right)^4\right) + 777.679; \quad \eta_g = 0.1, \tag{4.5.7}$$

$$M_{BH}(c) = 13838.729 \times \exp\left(-\left(\frac{c}{3966.455}\right)^4\right) + 829.899; \quad \eta_g = 0.3, \tag{4.5.8}$$

$$M_{BH}(c) = 16096.442 \times \exp\left(-\left(\frac{c}{3814.199}\right)^4\right) + 897.747; \quad \eta_g = 0.5, \tag{4.5.9}$$

$$M_{BH}(c) = 17766.999 \times \exp\left(-\left(\frac{c}{3480.472}\right)^4\right) + 645.66; \quad \eta_g = 1.0. \tag{4.5.10}$$

To extrapolate the final BH seed mass to the real value of the speed of light, we can use the equations provided above, considering $c = 3 \times 10^5$ km/s as listed in Table 4.5.1. We note that the trend becomes nearly flat for higher values of the speed of light. Furthermore, as the simulations only reach 10% of the real value of the speed of light, we could overestimate the inspiral time scale for high values of speed of light.

The ratio of the mass of the BH seed over the number of the mergers is given by α. This value gives us information of how many of the mergers feed the BH seed. If the value is equal to 1 it mean that all mergers of BHs in the cluster end in the BH seed. On the other hand, if the value is 0, it means none of the mergers feeds the BH seed. Formally we have

$$\alpha = \frac{M_{BH}}{10} \frac{1}{\text{Mergs}}. \tag{4.5.11}$$

In Fig 4.5.2, the values for α are presented. In the bottom-left panel, we can observe how, for lower values of $c < 3 \times 10^3$ km/s, α consistently remains above 0.9. This indicates that over 90% of BH mergers contribute to the growth of the BH seed. A similar trend is observed for a speed of light of 3×10^4 km/s, where even at higher external potentials, α remains high.

However, as we increase the speed of light, especially in the range between 6×10^3 and 10^4 km/s, α experiences a significant decline. This suggests that a substantial portion of BH binary mergers do not contribute to increasing the BH seed mass. This contrasts with the situation at a speed of light of 3×10^4 km/s, where α consistently remains above 0.8, indicating that most mergers involve the BH seed. Though clusters with 3×10^4 km/s form a similar mass BH seed as clusters with 6×10^3 and 10^4 km/s, which means we have some BHs with masses $> 10\,M_\odot$ that do not have the time nor the conditions to mergers with the BH seed.

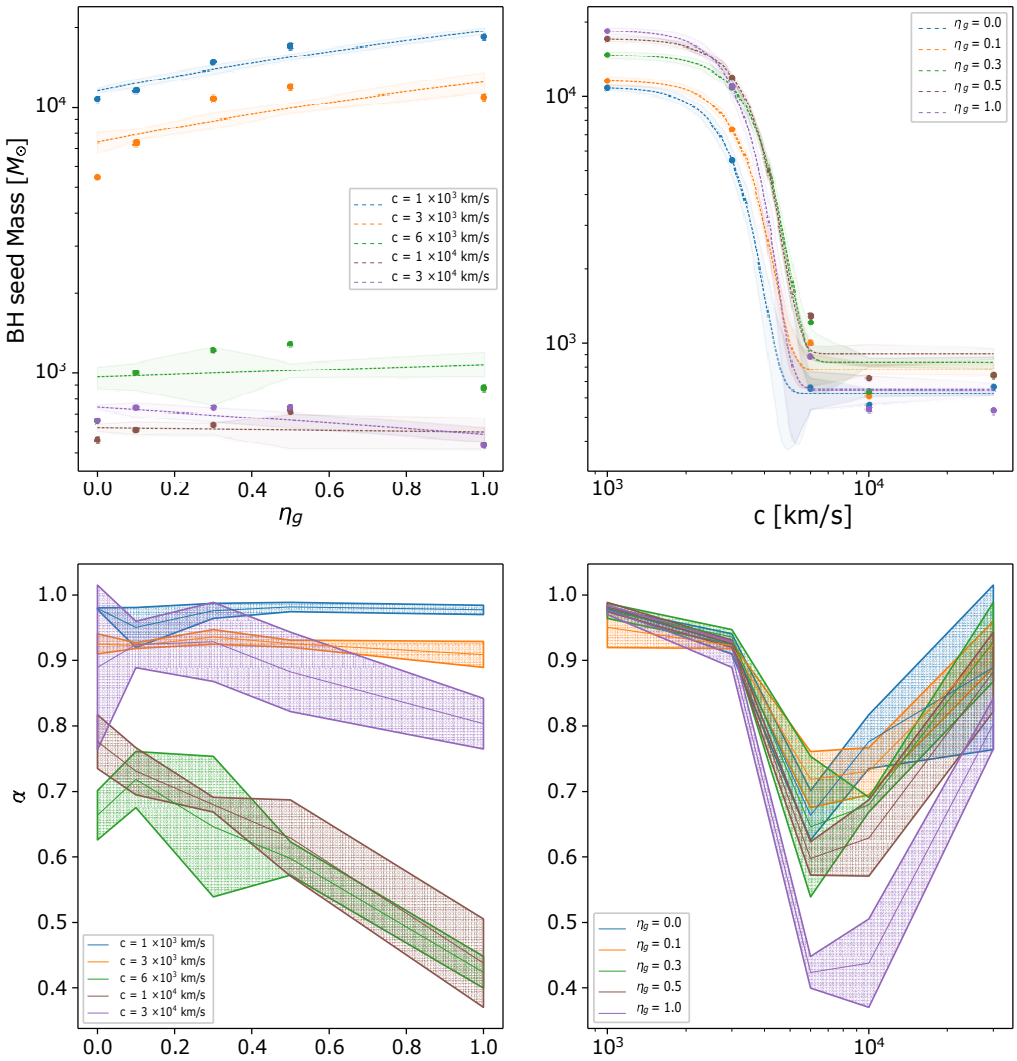

Figure 4.5.2: At the top we have the mass of the massive BH in the cluster at the end of the simulation. On the left panel, as a function of the external potential (η_g), different colors mark different speeds of light. On the right panel, we have the mass of the massive BH as a function of the light speed (c), with different colors marking the external potential. On the bottom we provide the ratio of amount of black holes that merger with BH seed and the mergers on the cluster defined α see eq. 4.5.11, and on the left panel as a function of the external potential. On the right panel we have α as a function of the speed of light.

Table 4.5.1: Extrapolation of the BHs seed mass as to the real value of the speed of the light 300.000km/s.

η_g	BH seed mass [$M_\odot$]
0.0	624.143 ± 14.142
0.1	777.678 ± 53.874
0.3	829.899 ± 83.301
0.5	897.747 ± 35.483
1.0	645.66 ± 20.355

4.6 Extrapolation to real clusters

As mentioned earlier, the principal condition for a black hole cluster to form a massive central black hole is that it needs to reach a relativistic state (i.e., $v_\infty \gtrsim 0.01c$). This condition is typically influenced by the density of the cluster, determined by its mass and radius. In our model, this condition is further impacted by the parameter η_g, representing the amount of gas accreted onto the black hole cluster. The accretion of gas increases the density of the cluster, consequently raising the root mean square velocity in the central regions, as expressed by (Binney and Tremaine, 2008). Considering the external potential, we can rewrite this velocity as:

$$v_\infty \approx \sqrt{0.4 \frac{GM_{BHs}(1+\eta_g)}{R_{vir}}}. \tag{4.6.1}$$

v_∞ does not adequately account for the contraction of the black hole cluster due to gas accretion. Therefore, the cluster is less dense than considered in the model proposed by Davies et al. (2011), where gas accretion affects the density of the cluster and subsequently influences the root mean square velocity. A more accurate velocity dispersion for a cluster affected by gas accretion is presented in (Kroupa et al., 2020) as

$$\sigma = \left(f_v \frac{GM_{BHs}^2 (1+\eta_g)^2}{R_{vir} M_{BHs}} \right)^{1/2}, \tag{4.6.2}$$

where M_{BHs} is the mass of BH in the cluster, R_{vir} is the virial radius and f_v is a dimensionless factor that covers a departure from the virial equilibrium or a

Table 4.5.2: In this table, we present characteristic results for the clusters corresponding to the initial conditions index in Table 3.7.1. The first column displays the mass of the BH seed at the end of the simulation, measured in solar masses. In the second column, we provide the number of mergers that occurred in the cluster. The third column indicates the time of core collapse, measured in millions of years (Myr). Finally, the last column presents the number of BH escapers in the cluster.

IDs	BH mass [$M_\odot$]	Mergers	T cc [Myr]	Escapers
1	10730 ± 255	1095 ± 26	84.65±4.93	2063.25±32.13
2	11495 ± 485	1209 ± 19	107.66±5.755	2598±8.831
3	14635 ± 526	1499 ± 37	162.30±16.134	2369.5 ±25.02
4	16930 ± 427	1724 ± 32	231.40±20.465	1764.5±23.7
5	18005 ± 700	1857 ± 57	443.3±9.428	650.66±37.24
6	5460 ± 675	590 ± 77	89.13±5.293	2221.75±302.46
7	7317 ± 382	793 ± 40	133±4.446	2552±23.04
8	10770 ± 599	1150 ± 54	217.10±10.154	2433.5±10.11
9	11857 ± 469	1281 ± 43	336.40±4.299	1894.55±24.08
10	11333 ± 875.9	1238 ± 67	755.58±21.065	570.6±4.78
11	655 ± 90.6	98.5 ± 11	103.12±3.420	2678±55.33
12	997 ± 114.7	138.7 ± 12	139.34±4.367	3016.5±142.68
13	1207.5 ± 247.3	185.75 ± 8	230.23±8.687	2739.25±188.95
14	1282.5 ± 65.7	214.75 ± 11	384.35±5.866	2179.25±51.36
15	916.6 ± 102.0	212.3 ± 13	909.03±44.405	585.663±5.55
16	557 ± 20	72 ± 3	103.86±4.045	2648.25±42.86
17	605 ± 35	82 ± 1	142.51±4.602	3141.±28.77
18	632 ± 31	93 ± 3	241.92±3.86	2823.5±10.97
19	715 ± 92	113 ± 7	388.54±11.63	2029.25±57.603
20	570 ± 63	122 ± 4	1043.81±44.99	558.66±10.14
21	660 ± 14.1	76 ± 12	104.79±4.83	2553.5±84.913
22	735 ± 43.8	79.5 ± 3	141.24±4.52	2826±80.28
23	735 ± 43.3	79.25 ± 2	248.17±11.82	2460±62.95
24	737.5 ± 45.4	84 ± 7	411.05±7.574	1823±38.79
25	546.6 ± 23.5	69.3 ± 4	1178.19±29.093	554.33±0.471

particular shape of the potential well.

In Fig.4.6.1, we present the trends of the velocity for the two models considering different external potentials (η_g). On the top panel, we have the model considering that the cluster is not shrunk by the accretion gas, where only clusters with a gas mass ratio of $\eta_g = 5.0$ and very dense clusters with a radius of $R_{vir} = 0.25$ pc and masses of approximately $\approx 8 \times 10^7\ M_\odot$ reach the velocity necessary to be considered in a relativistic state.

On the other hand, the second panel shows the velocity considering that the cluster is shrunk by the gas accretion. Here, we can observe that more clusters reach the velocities necessary to be in a relativistic state, with lower masses of approximately $\approx 2 \times 10^7\ M_\odot$ and higher radii $R_{vir} = 1$ pc, even for clusters with an external potential of $\eta_g = 0.3$. It is important to note that this consideration is based on the initial conditions, and during their evolution, clusters could attain higher velocities, allowing clusters with lower masses to reach a relativistic state in the inner regions, as shown by Kroupa et al. (2020).

In Fig. 4.6.2, the efficiency (ϵ) of the cluster to form a massive object is depicted as the ratio between the mass of the cluster $M_{\rm cluster} = M_{\rm BHs}(1 + \eta_g)$ and the mass of the central massive BH, plotted against the ratio between the velocity dispersion at the time of the core contraction and the speed of light considered in the simulation. As v_∞/c increases, the efficiency of the cluster to form a massive object also increases, reaching a high efficiency of around $\epsilon = 0.06$ for speed of light $\leq 6 \times 10^3$km/s and $\epsilon = 0.08$ for speed of light of $> 6 \times 10^3$km/s. The external potential has an influence on the efficiency, with clusters having external potentials of $\eta_g = 0.3 - 0.5$ exhibiting the highest efficiency, while clusters with an external potential of $\eta_g = 1.0$ showing lower efficiencies. This is attributed to the time required to reach core contraction, as discussed earlier. Clusters not in a relativistic state have an efficiency in the range of ≈ 0.003, where approximately $\approx 0.3\%$ of the mass of the cluster forms the central BH. In contrast, clusters in a relativistic state exhibit an efficiency of ≈ 0.05, with around $\approx 5\%$ of the mass of the cluster forming a central massive BH.

Considering the mass and radius of the cluster, we compute their rms velocities with equations 4.6.1 and 4.6.2. If we take the ratio between velocity and the real speed of light $c = 3 \times 10^5$ km/s, we can associate an efficiency, as shown in Fig.

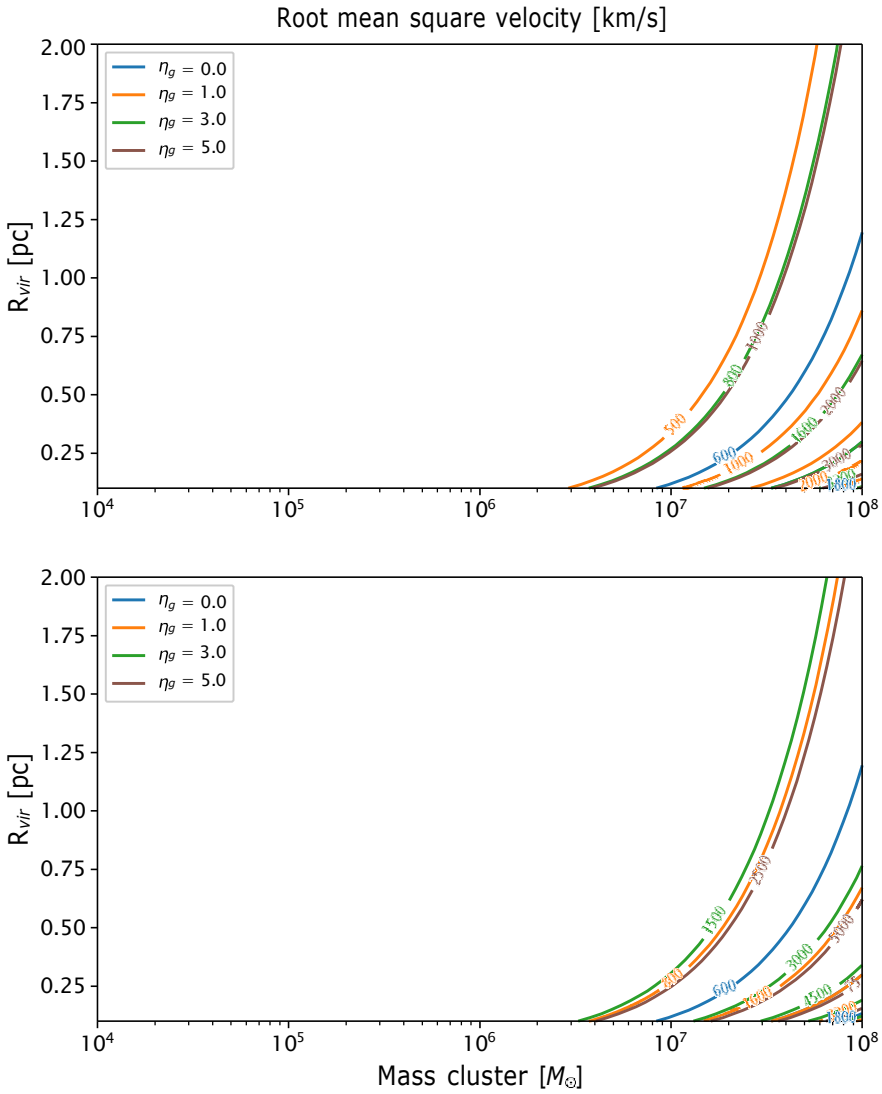

Figure 4.6.1: In the top panel, we depict rms contour lines of the velocity calculated by Equation 4.6.1, showcasing its dependency on the virial radius and the mass of BHs in the cluster. The contours illustrate the velocities at specific radii and masses. Meanwhile, the bottom panel illustrates countour lines of the velocity of the cluster including as defined by Equation 4.6.2, where different colors indicate various values of η_g.

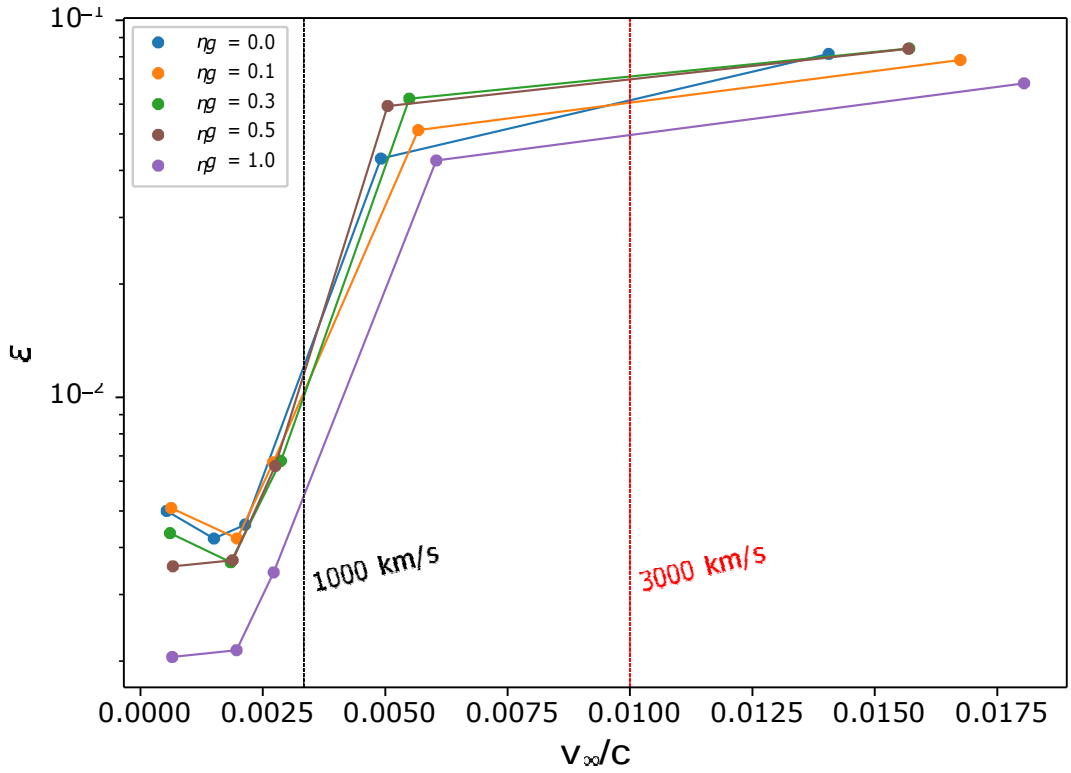

Figure 4.6.2: We present the BH formation efficiency of the clusters defined as the mass of the most massive BH divided by the total mass of the cluster, as a function of the ratio between the root mean square (rms) velocity at the time of the core collapse and the speed of light (c), as considered in the simulations. Different colors are used to denote varying external potentials η_g. The vertical lines mark velocity to ratios assuming the real value of the speeed of light of clusters with an rms velocity of 1000 km/s and 3000 km/s

4.6.2. In Fig. 4.6.3, we compute the final mass of massive BHs that could form, considering their velocities and the associated efficiency. In this plot, we consider the velocities given by Eq. 4.6.2 also consider different values of the external potential of 0.0, 0.3, 0.5, 1.0. We consider a cluster mass range of $10^4 - 10^8\,M_\odot$ and radii of $0.1 - 2$ pc. We can note that for clusters with less than $\approx 10^{4.3}\,M_\odot$, the clusters only form BHs with masses around $10^2\,M_\odot$, independent of the external potential considered. further we note the behavior for all external potentials where at lower R_{vir} the efficiency increase. For clusters with masses of $\approx 10^6 - 10^7\,M_\odot$ and $\eta_g = 0.0 - 0.3$, they can form massive BHs with masses of $\approx 10^4 - 10^5\,M_\odot$. For higher-mass clusters, i.e., $\approx 10^7 - 10^{7.5}\,M_\odot$, they are considered relativistic clusters with small radii lower than 0.25 pc, and this holds true for all clusters, regardless of the external potential. Clusters with a radius of 1.0 pc need high masses, $\approx 10^8\,M_\odot$, and $\eta_g = 1.0$ to be in a relativistic state, forming more massive BHs.

When we consider the velocity given in equation 4.6.2, we observe how the external potential has a high impact on the velocity in the cluster. This leads to the formation of more massive BHs with lower masses and for higher radii, unlike clusters without external potential where both velocities are equal. The most significant difference is observed in clusters with an external potential of $\eta_g = 1.0$, where the clusters are in a relativistic state for masses in the range of $\approx 10^{6.5} - 10^{7.5}\,M_\odot$ and for radii in the range of $0.25 - 1.0$ pc. In this scenario, the cluster can form massive BHs with an efficiency comparable to that of a relativistic cluster.

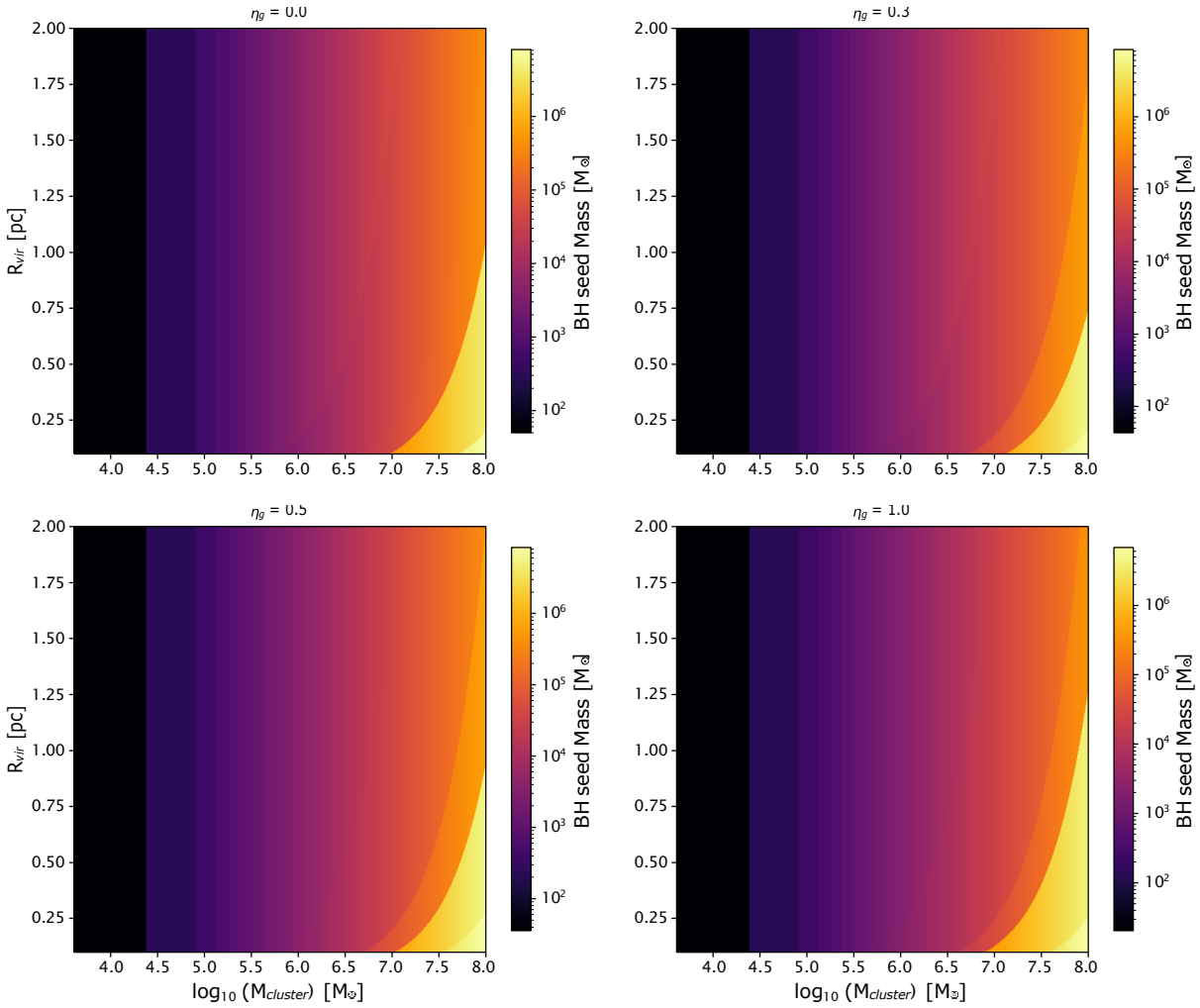

Figure 4.6.3: We display the black holes (BHs) that can form clusters based on root mean square (rms) velocities calculated using equation 4.6.1 and their corresponding efficiency depicted in Fig. 4.6.2. The clusters are within a range of virial radii from 0.1 to 2.0 pc and masses from 10^4 - 10^8 $M_\odot$. The color represents the mass of the BHs that form the clusters, and each panel corresponds to different external potentials.

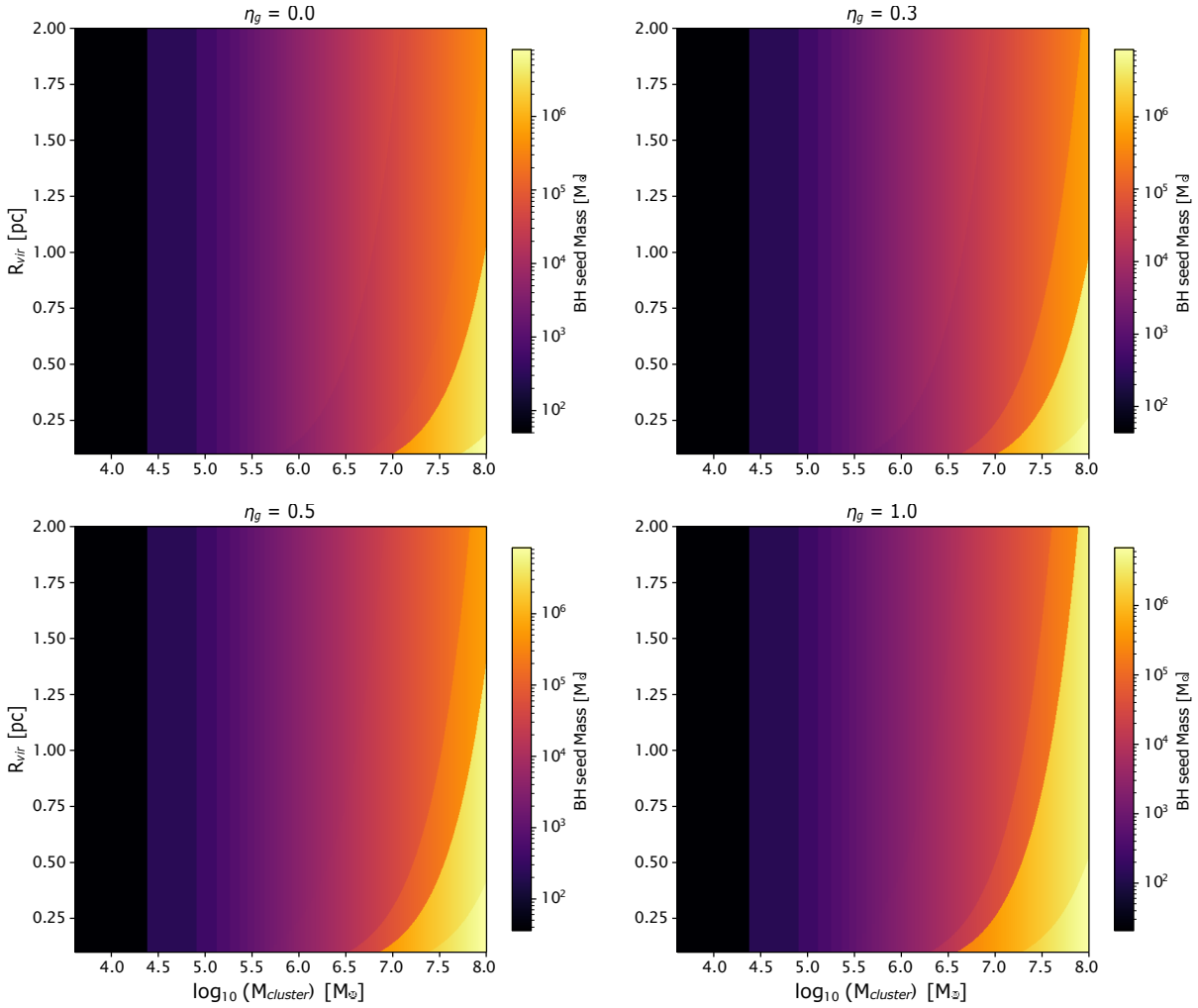

Figure 4.6.4: We display the black holes (BHs) that can form clusters based on root mean square (rms) velocities calculated using equation 4.6.2 (Kroupa et al., 2020) and their corresponding efficiency depicted in Fig. 4.6.2. The clusters are within a range of virial radii from 0.1 - 2.0 pc and masses from 10^4 - 10^8 $M_\odot$. The color represents the mass of the BHs that form the clusters, and each panel corresponds to different external potentials.

Chapter 5

Conclusion

In this thesis, we conducted a comprehensive study on the formation of Intermediate Mass Black Holes (IMBHs) in nuclear star clusters through runaway mergers of Black Holes (BHs). Our investigation focuses on the evolution of BH clusters in the presence of gas, focusing on the scenario outlined by Davies et al. (2011). The study aims to elucidate how the core of the NSC evolves and the formation of massive BH seeds .

To explore this model, we conducted a series of simulations using the Nbody6++GPU code. In these simulations, we incorporated an analytic potential with varying values to analyze its impact on the evolution of the cluster. Furthermore, we manipulated the speed of light to expedite the BH mergers due to the computational expenses associated with these simulations.

In these simulations, our primary focus was on studying the core contraction, including the time when it occurs and the resulting densities. Additionally, we delved into the characteristics of the binary population, such as their semi-major axis and eccentricities. Exploring the ejections from the cluster, BH-BH mergers, and the evolution of the BH seed were also integral aspects of our investigation. The key findings and insights from our results can be summarized in the following topics:

- The first result of our simulations, shown in Figure 4.1.4, is the time of core contraction in relaxation times as a function of the external potential. We observe a clear trend where the time of highest density or core contraction increases with higher external potential, consistent with findings in Reinoso

et al. (2020). However, for lower values of c, the behavior is different, with the time core contraction tending to decrease or remain constant as the external potential increases. This is attributed to the cluster having the root mean square (rms) velocity necessary to enter a relativistic stage or be in proximity to it, aligning with similar results obtained by Kupi et al. (2006).

- Binary formation by three body encounters in the cluster tends to produce more tight binaries when increasing the external potential, reducing the semi-mayor axis. On the other hand, the eccentricities of the binaries tend to not have a big difference between clusters with the same speed of light, but with different external potentials. The only big difference is in the overall reduction of the binary population when increasing the external potential.

- The number of escapers in the cluster, whether through evaporation or ejections, tends to decrease with higher external potentials. In clusters with lower gas mass fractions (η_g), the mass loss reaches around 20%, while in clusters with a high external potential of $\eta_g = 1.0$, the mass loss is only around 5%.

- Clusters in a relativistic state or near it are capable of producing BH seeds in a mass range of approximately $10^4 M_\odot$, experiencing a twofold increase in mass with higher external potential with efficiencies $\approx 10^{-1}$. In contrast, clusters far from a relativistic state can only produce BH seeds of approximately $10^3 M_\odot$ with efficiencies $\approx 10^{-2}$. This aligns with the findings from Kupi et al. (2006), where clusters in a relativistic state exhibit a BH seed mass of 6% of the total initial mass of the cluster. Similar models also support these results, as seen in Fragione and Silk (2020), who consider denser Nuclear Star Clusters (NSC) and account for gravitational wave recoil effects.

- To resemble real clusters, as anticipated, we require clusters that are denser to achieve a relativistic state. They should also be more massive and have smaller radii, as indicated by the yellow regions in Fig. 4.6.3 - 4.6.4. Additionally, the way of including the external potential significantly affects the rms velocity of the cluster and the BH formation efficiency. For clusters in equilibrium with the external potential, it is more difficult to form massive BHs, while a contraction of the cluster due to the inflow will favor the process.

In a cluster with a virial radius of $R_{vir} = 0.1 - 2.0$ pc and masses of 10^4 and 6×10^4 $M_\odot$, a central black hole of 100 $M_\odot$ can form. To form a central black hole of 10^3 $M_\odot$, the cluster needs a virial radius of $R_{vir} = 0.1 - 2.0$ pc and masses of $17 \times 10^4 - 24 \times 10^4$ $M_\odot$. Finally, to form a central black hole with masses between $10^4 - 10^5$ $M_\odot$, the cluster needs a virial radius of $R_{vir} = 0.1 - 2.0$ pc and a mass of $2 \times 10^6 - 2.4 \times 10^6$ $M_\odot$. The radii begin to constrain the formation of high-mass black holes in lower-mass clusters.

Chapter 6

Discussion and future work

This investigation provides a clear insight into the formation of an Intermediate Mass Black Hole (IMBH) in the dark core of a Nuclear Star Cluster (NSC). In a simplified model, we consider a cluster with equal mass BHs distributed according to a Plummer distribution. In our simulations, we form two sets of BH seeds, approximately 10^4 for clusters in a relativistic state and approximately 10^3 for other clusters.

However, our models are affected by certain non-realistic assumptions. For instance, assuming equal-mass BHs in the cluster impacts mass segregation, leading to time scales for cluster evolution higher than reality, for instance in clusters with a realistic stellar mass function the $t_{cc} \backsimeq 0.2 t_{rh}$ (Zwart and McMillan, 2002).

Additionally, we neglect gas accretion onto the BHs, which way affect the time scale evolution, including the relaxation time (Leigh et al., 2013) and the mass distribution of the BHs in the cluster. Furthermore, gravitational recoil caused by gravitational waves is not considered in the simulation. Recent versions of Nbody6++gpu include these effects. Studies such as Fragione and Silk (2020) provide a more extensive analysis of mergers and escapers considering recoils, with velocities upto a few thousand km, where the typical mass of an ejected massive BH is 400-500 $M_\odot$. They also explore how the mass and density of the NSC influences the retention of massive BHs and the formation of binaries, where the massive NSCs can more easily retain massive BHs but the formation of binaries requires longer time scales. Dense NSCs both can retain massive BHs and have a higher efficiency in forming binaries that merge through GW emission.

Regarding future work on the formation of an IMBH in a realistic NSC, Kroupa et al. (2020) demonstrate that for a high mass ratio of gas, $\eta_g > 5.78$, the cluster tends to expand for dark core masses $< 10^7 M_\odot$. However, for a mass of the dark core $> 10^7\ M_\odot$, the cluster is already initially in a relativistic state, on a large scale of the cluster. To form an IMBH, we could consider massive dark cores with either massive black holes $> 10\ M_\odot$ or a higher number of BHs in the cluster. But this is not enough to reach the core collapse with the methodology that we use so far, as the relaxation time scales as $\propto (1 + \eta_g)^4$, so for higher than $\eta_g = 2.0$ the core collapse will require more than 1.4 Gyr. We further note that an initial mass distribution of the BHs could reduce the time of the core collapse. Of course, this is a recent investigation and our knowledge on the mass distribution of stellar mass BHs is still limited, and no model can fully reproduce the distribution of observed total masses. Nevertheless, the observations lie within the distribution of mass in 1σ band of the $M_{max} = 50\ M_\odot$, $\alpha = 2.35$ model (Perna et al., 2019). which could be employed in the follow-up calculations in the future. In future projects it will also important to understand resonant relaxation (or Kozai) effects, which could significantly increase the rate of inspiral and their relation with the PN 1 and PN 2, affecting the precession and the impact of the number of captures (Hopman and Alexander, 2006). Finally, the consideration of radiation recoils will give us a better understanding of the evolution and the formation of an IMBH.

Bibliography

Aarseth, S. J. (1985). Direct methods for n-body simulations. In *Multiple time scales*, pages 377–418. Elsevier.

Aarseth, S. J. (2007). Post-Newtonian N-body simulations. *Monthly Notices of the Royal Astronomical Society*, 378(1):285–292.

Aarseth, S. J. and Hoyle, F. (1963). Dynamical Evolution of Clusters of Galaxies, I. *Monthly Notices of the Royal Astronomical Society*, 126(3):223–255.

Ahmad, A. and Cohen, L. (1973). A numerical integration scheme for the n-body gravitational problem. *Journal of Computational Physics*, 12(3):389–402.

Alexander, T. and Natarajan, P. (2014). Rapid growth of seed black holes in the early universe by supra-exponential accretion. *Science*, 345(6202):1330–1333.

Bañados, E., Venemans, B. P., Decarli, R., Farina, E. P., Mazzucchelli, C., Walter, F., Fan, X., Stern, D., Schlafly, E., Chambers, K. C., Rix, H. W., Jiang, L., McGreer, I., Simcoe, R., Wang, F., Yang, J., Morganson, E., De Rosa, G., Greiner, J., Baloković, M., Burgett, W. S., Cooper, T., Draper, P. W., Flewelling, H., Hodapp, K. W., Jun, H. D., Kaiser, N., Kudritzki, R. P., Magnier, E. A., Metcalfe, N., Miller, D., Schindler, J. T., Tonry, J. L., Wainscoat, R. J., Waters, C., and Yang, Q. (2016). The Pan-STARRS1 Distant z > 5.6 Quasar Survey: More than 100 Quasars within the First Gyr of the Universe. , 227(1):11.

Bañados, E., Venemans, B. P., Mazzucchelli, C., Farina, E. P., Walter, F., Wang, F., Decarli, R., Stern, D., Fan, X., Davies, F. B., Hennawi, J. F., Simcoe, R. A., Turner, M. L., Rix, H.-W., Yang, J., Kelson, D. D., Rudie, G. C., and Winters, J. M. (2018). An 800-million-solar-mass black hole in a significantly neutral Universe at a redshift of 7.5. , 553(7689):473–476.

Banerjee, S. and Kroupa, P. (2011). A New Type of Compact Stellar Population: Dark Star Clusters. , 741(1):L12.

Begelman, M. C. (2010). Evolution of supermassive stars as a pathway to black hole formation. *Monthly Notices of the Royal Astronomical Society*, 402(1):673–681.

Begelman, M. C., Volonteri, M., and Rees, M. J. (2006). Formation of supermassive black holes by direct collapse in pre-galactic haloes. *Monthly Notices of the Royal Astronomical Society*, 370(1):289–298.

Bellovary, J., Volonteri, M., Governato, F., Shen, S., Quinn, T., and Wadsley, J. (2011). The First Massive Black Hole Seeds and Their Hosts. , 742(1):13.

Bender, R., Kormendy, J., Bower, G., Green, R., Thomas, J., Danks, A. C., Gull, T., Hutchings, J. B., Joseph, C. L., Kaiser, M. E., Lauer, T. R., Nelson, C. H., Richstone, D., Weistrop, D., and Woodgate, B. (2005). HST STIS Spectroscopy of the Triple Nucleus of M31: Two Nested Disks in Keplerian Rotation around a Supermassive Black Hole. , 631(1):280–300.

Binney, J. and Tremaine, S. (2008). *Galactic Dynamics: Second Edition*.

Breen, P. G. and Heggie, D. C. (2013). Dynamical evolution of black hole subsystems in idealized star clusters. , 432(4):2779–2797.

Bromm, V. and Loeb, A. (2003). Formation of the First Supermassive Black Holes. , 596(1):34–46.

Chandrasekhar, S. (1964). The Dynamical Instability of Gaseous Masses Approaching the Schwarzschild Limit in General Relativity. , 140:417.

Davies, M. B., Miller, M. C., and Bellovary, J. M. (2011). Supermassive Black Hole Formation Via Gas Accretion in Nuclear Stellar Clusters. , 740(2):L42.

Devecchi, B. and Volonteri, M. (2009). FORMATION OF THE FIRST NUCLEAR CLUSTERS AND MASSIVE BLACK HOLES AT HIGH REDSHIFT. *The Astrophysical Journal*, 694(1):302–313.

Dijkstra, M., Haiman, Z., Mesinger, A., and Wyithe, J. S. B. (2008). Fluctuations in the high-redshift Lyman–Werner background: close halo pairs as the origin of supermassive black holes. *Monthly Notices of the Royal Astronomical Society*, 391(4):1961–1972.

Dressler, A. and Richstone, D. O. (1988). Stellar Dynamics in the Nuclei of M31 and M32: Evidence for Massive Black Holes. , 324:701.

Escala, A. (2021). Observational Support for Massive Black Hole Formation Driven by Runaway Stellar Collisions in Galactic Nuclei. , 908(1):57.

Event Horizon Telescope Collaboration, Akiyama, K., Alberdi, A., Alef, W., Algaba, J. C., Anantua, R., Asada, K., Azulay, R., Bach, U., Baczko, A.-K., Ball, D., Baloković, M., Barrett, J., Bauböck, M., Benson, B. A., Bintley, D., Blackburn, L., Blundell, R., Bouman, K. L., Bower, G. C., Boyce, H., Bremer, M., Brinkerink, C. D., Brissenden, R., Britzen, S., Broderick, A. E., Broguiere, D., Bronzwaer, T., Bustamante, S., Byun, D.-Y., Carlstrom, J. E., Ceccobello, C., Chael, A., Chan, C.-k., Chatterjee, K., Chatterjee, S., Chen, M.-T., Chen, Y., Cheng, X., Cho, I., Christian, P., Conroy, N. S., Conway, J. E., Cordes, J. M., Crawford, T. M., Crew, G. B., Cruz-Osorio, A., Cui, Y., Davelaar, J., De Laurentis, M., Deane, R., Dempsey, J., Desvignes, G., Dexter, J., Dhruv, V., Doeleman, S. S., Dougal, S., Dzib, S. A., Eatough, R. P., Emami, R., Falcke, H., Farah, J., Fish, V. L., Fomalont, E., Ford, H. A., Fraga-Encinas, R., Freeman, W. T., Friberg, P., Fromm, C. M., Fuentes, A.,

Galison, P., Gammie, C. F., García, R., Gentaz, O., Georgiev, B., Goddi, C., Gold, R., Gómez-Ruiz, A. I., Gómez, J. L., Gu, M., Gurwell, M., Hada, K., Haggard, D., Haworth, K., Hecht, M. H., Hesper, R., Heumann, D., Ho, L. C., Ho, P., Honma, M., Huang, C.-W. L., Huang, L., Hughes, D. H., Ikeda, S., Impellizzeri, C. M. V., Inoue, M., Issaoun, S., James, D. J., Jannuzi, B. T., Janssen, M., Jeter, B., Jiang, W., Jiménez-Rosales, A., Johnson, M. D., Jorstad, S., Joshi, A. V., Jung, T., Karami, M., Karuppusamy, R., Kawashima, T., Keating, G. K., Kettenis, M., Kim, D.-J., Kim, J.-Y., Kim, J., Kim, J., Kino, M., Koay, J. Y., Kocherlakota, P., Kofuji, Y., Koch, P. M., Koyama, S., Kramer, C., Kramer, M., Krichbaum, T. P., Kuo, C.-Y., La Bella, N., Lauer, T. R., Lee, D., Lee, S.-S., Leung, P. K., Levis, A., Li, Z., Lico, R., Lindahl, G., Lindqvist, M., Lisakov, M., Liu, J., Liu, K., Liuzzo, E., Lo, W.-P., Lobanov, A. P., Loinard, L., Lonsdale, C. J., Lu, R.-S., Mao, J., Marchili, N., Markoff, S., Marrone, D. P., Marscher, A. P., Martí-Vidal, I., Matsushita, S., Matthews, L. D., Medeiros, L., Menten, K. M., Michalik, D., Mizuno, I., Mizuno, Y., Moran, J. M., Moriyama, K., Moscibrodzka, M., Müller, C., Mus, A., Musoke, G., Myserlis, I., Nadolski, A., Nagai, H., Nagar, N. M., Nakamura, M., Narayan, R., Narayanan, G., Natarajan, I., Nathanail, A., Fuentes, S. N., Neilsen, J., Neri, R., Ni, C., Noutsos, A., Nowak, M. A., Oh, J., Okino, H., Olivares, H., Ortiz-León, G. N., Oyama, T., Özel, F., Palumbo, D. C. M., Paraschos, G. F., Park, J., Parsons, H., Patel, N., Pen, U.-L., Pesce, D. W., Piétu, V., Plambeck, R., PopStefanija, A., Porth, O., Pötzl, F. M., Prather, B., Preciado-López, J. A., Psaltis, D., Pu, H.-Y., Ramakrishnan, V., Rao, R., Rawlings, M. G., Raymond, A. W., Rezzolla, L., Ricarte, A., Ripperda, B., Roelofs, F., Rogers, A., Ros, E., Romero-Cañizales, C., Roshanineshat, A., Rottmann, H., Roy, A. L., Ruiz, I., Ruszczyk, C., Rygl, K. L. J., Sánchez, S., Sánchez-Argüelles, D., Sánchez-Portal, M., Sasada, M., Satapathy, K., Savolainen, T., Schloerb, F. P., Schonfeld, J., Schuster, K.-F., Shao, L., Shen, Z., Small, D., Sohn, B. W., SooHoo, J., Souccar, K., Sun, H., Tazaki, F., Tetarenko, A. J., Tiede, P., Tilanus, R. P. J., Titus, M., Torne, P., Traianou, E., Trent, T., Trippe, S., Turk, M., van Bemmel, I., van Langevelde, H. J., van Rossum, D. R., Vos, J., Wagner, J., Ward-Thompson, D., Wardle, J., Weintroub, J., Wex, N., Wharton, R., Wielgus, M., Wiik, K., Witzel, G., Wondrak, M. F., Wong, G. N., Wu, Q., Yamaguchi, P., Yoon, D., Young, A., Young, K., Younsi, Z., Yuan, F., Yuan, Y.-F., Zensus, J. A., Zhang, S., Zhao, G.-Y., Zhao, S.-S., Agurto, C., Allardi, A., Amestica, R., Araneda, J. P., Arriagada, O., Berghuis, J. L., Bertarini, A., Berthold, R., Blanchard, J., Brown, K., Cárdenas, M., Cantzler, M., Caro, P., Castillo-Domínguez, E., Chan, T. L., Chang, C.-C., Chang, D. O., Chang, S.-H., Chang, S.-C., Chen, C.-C., Chilson, R., Chuter, T. C., Ciechanowicz, M., Colin-Beltran, E., Coulson, I. M., Crowley, J., Degenaar, N., Dornbusch, S., Durán, C. A., Everett, W. B., Faber, A., Forster, K., Fuchs, M. M., Gale, D. M., Geertsema, G., González, E., Graham, D., Gueth, F., Halverson, N. W., Han, C.-C., Han, K.-C., Hasegawa, Y., Hernández-Rebollar, J. L., Herrera, C., Herrero-Illana, R., Heyminck, S., Hirota, A., Hoge, J., Hostler Schimpf, S. R., Howie, R. E., Huang, Y.-D., Jiang, H., Jinchi, H., John, D., Kimura, K., Klein,

T., Kubo, D., Kuroda, J., Kwon, C., Lacasse, R., Laing, R., Leitch, E. M., Li, C.-T., Liu, C.-T., Liu, K.-Y., Lin, L. C. C., Lu, L.-M., Mac-Auliffe, F., Martin-Cocher, P., Matulonis, C., Maute, J. K., Messias, H., Meyer-Zhao, Z., Montaña, A., Montenegro-Montes, F., Montgomerie, W., Moreno Nolasco, M. E., Muders, D., Nishioka, H., Norton, T. J., Nystrom, G., Ogawa, H., Olivares, R., Oshiro, P., Pérez-Beaupuits, J. P., Parra, R., Phillips, N. M., Poirier, M., Pradel, N., Qiu, R., Raffin, P. A., Rahlin, A. S., Ramírez, J., Ressler, S., Reynolds, M., Rodríguez-Montoya, I., Saez-Madain, A. F., Santana, J., Shaw, P., Shirkey, L. E., Silva, K. M., Snow, W., Sousa, D., Sridharan, T. K., Stahm, W., Stark, A. A., Test, J., Torstensson, K., Venegas, P., Walther, C., Wei, T.-S., White, C., Wieching, G., Wijnands, R., Wouterloot, J. G. A., Yu, C.-Y., Yu , W., and Zeballos, M. (2022). First Sagittarius A* Event Horizon Telescope Results. I. The Shadow of the Supermassive Black Hole in the Center of the Milky Way. , 930(2):L12.

Event Horizon Telescope Collaboration, Akiyama, K., Alberdi, A., Alef, W., Asada, K., Azulay, R., Baczko, A.-K., Ball, D., Baloković, M., Barrett, J., Bintley, D., Blackburn, L., Boland, W., Bouman, K. L., Bower, G. C., Bremer, M., Brinkerink, C. D., Brissenden, R., Britzen, S., Broderick, A. E., Broguiere, D., Bronzwaer, T., Byun, D.-Y., Carlstrom, J. E., Chael, A., Chan, C.-k., Chatterjee, S., Chatterjee, K., Chen, M.-T., Chen, Y., Cho, I., Christian, P., Conway, J. E., Cordes, J. M., Crew, G. B., Cui, Y., Davelaar, J., De Laurentis, M., Deane, R., Dempsey, J., Desvignes, G., Dexter, J., Doeleman, S. S., Eatough, R. P., Falcke, H., Fish, V. L., Fomalont, E., Fraga-Encinas, R., Freeman, W. T., Friberg, P., Fromm, C. M., Gómez, J. L., Galison, P., Gammie, C. F., García, R., Gentaz, O., Georgiev, B., Goddi, C., Gold, R., Gu, M., Gurwell, M., Hada, K., Hecht, M. H., Hesper, R., Ho, L. C., Ho, P., Honma, M., Huang, C.-W. L., Huang, L., Hughes, D. H., Ikeda, S., Inoue, M., Issaoun, S., James, D. J., Jannuzi, B. T., Janssen, M., Jeter, B., Jiang, W., Johnson, M. D., Jorstad, S., Jung, T., Karami, M., Karuppusamy, R., Kawashima, T., Keating, G. K., Kettenis, M., Kim, J.-Y., Kim, J., Kim, J., Kino, M., Koay, J. Y., Koch, P. M., Koyama, S., Kramer, M., Kramer, C., Krichbaum, T. P., Kuo, C.-Y., Lauer, T. R., Lee, S.-S., Li, Y.-R., Li, Z., Lindqvist, M., Liu, K., Liuzzo, E., Lo, W.-P., Lobanov, A. P., Loinard, L., Lonsdale, C., Lu, R.-S., MacDonald, N. R., Mao, J., Markoff, S., Marrone, D. P., Marscher, A. P., Martí-Vidal, I., Matsushita, S., Matthews, L. D., Medeiros, L., Menten, K. M., Mizuno, Y., Mizuno, I., Moran, J. M., Moriyama, K., Moscibrodzka, M., Müller, C., Nagai, H., Nagar, N. M., Nakamura, M., Narayan, R., Narayanan, G., Natarajan, I., Neri, R., Ni, C., Noutsos, A., Okino, H., Olivares, H., Ortiz-León, G. N., Oyama, T., Özel, F., Palumbo, D. C. M., Patel, N., Pen, U.-L., Pesce, D. W., Piétu, V., Plambeck, R., PopStefanija, A., Porth, O., Prather, B., Preciado-López, J. A., Psaltis, D., Pu, H.-Y., Ramakrishnan, V., Rao, R., Rawlings, M. G., Raymond, A. W., Rezzolla, L., Ripperda, B., Roelofs, F., Rogers, A., Ros, E., Rose, M., Roshanineshat, A., Rottmann, H., Roy, A. L., Ruszczyk, C., Ryan, B. R., Rygl, K. L. J., Sánchez, S., Sánchez-Arguelles, D., Sasada, M., Savolainen, T., Schloerb, F. P., Schuster, K.-F., Shao, L., Shen, Z., Small, D.,

Sohn, B. W., SooHoo, J., Tazaki, F., Tiede, P., Tilanus, R. P. J., Titus, M., Toma, K., Torne, P., Trent, T., Trippe, S., Tsuda, S., van Bemmel, I., van Langevelde, H. J., van Rossum, D. R., Wagner, J., Wardle, J., Weintroub, J., Wex, N., Wharton, R., Wielgus, M., Wong, G. N., Wu, Q., Young, K., Young, A., Younsi, Z., Yuan, F., Yuan, Y.-F., Zensus, J. A., Zhao, G., Zhao, S.-S., Zhu, Z., Algaba, J.-C., Allardi, A., Amestica, R., Anczarski, J., Bach, U., Baganoff, F. K., Beaudoin, C., Benson, B. A., Berthold, R., Blanchard, J. M., Blundell, R., Bustamente, S., Cappallo, R., Castillo-Domínguez, E., Chang, C.-C., Chang, S.-H., Chang, S.-C., Chen, C.-C., Chilson, R., Chuter, T. C., Córdova Rosado, R., Coulson, I. M., Crawford, T. M., Crowley, J., David, J., Derome, M., Dexter, M., Dornbusch, S., Dudevoir, K. A., Dzib, S. A., Eckart, A., Eckert, C., Erickson, N. R., Everett, W. B., Faber, A., Farah, J. R., Fath, V., Folkers, T. W., Forbes, D. C., Freund, R., Gómez-Ruiz, A. I., Gale, D. M., Gao, F., Geertsema, G., Graham, D. A., Greer, C. H., Grosslein, R., Gueth, F., Haggard, D., Halverson, N. W., Han, C.-C., Han, K.-C., Hao, J., Hasegawa, Y., Henning, J. W., Hernández-Gómez, A., Herrero-Illana, R., Heyminck, S., Hirota, A., Hoge, J., Huang, Y.-D., Impellizzeri, C. M. V., Jiang, H., Kamble, A., Keisler, R., Kimura, K., Kono, Y., Kubo, D., Kuroda, J., Lacasse, R., Laing, R. A., Leitch, E. M., Li, C.-T., Lin, L. C. C., Liu, C.-T., Liu, K.-Y., Lu, L.-M., Marson, R. G., Martin-Cocher, P. L., Massingill, K. D., Matulonis, C., McColl, M. P., McWhirter, S. R., Messias, H., Meyer-Zhao, Z., Michalik, D., Montaña, A., Montgomerie, W., Mora-Klein, M., Muders, D., Nadolski, A., Navarro, S., Neilsen, J., Nguyen, C. H., Nishioka, H., Norton, T., Nowak, M. A., Nystrom, G., Ogawa, H., Oshiro, P., Oyama, T., Parsons, H., Paine, S. N., Peñalver, J., Phillips, N. M., Poirier, M., Pradel, N., Primiani, R. A., Raffin, P. A., Rahlin, A. S., Reiland, G., Risacher, C., Ruiz, I., Sáez-Madaín, A. F., Sassella, R., Schellart, P., Shaw, P., Silva, K. M., Shiokawa, H., Smith, D. R., Snow, W., Souccar, K., Sousa, D., Sridharan, T. K., Srinivasan, R., Stahm, W., Stark, A. A., Story, K., Timmer, S. T., Vertatschitsch, L., Walther, C., Wei, T.-S., Whitehorn, N., Whitney, A. R., Woody, D. P., Wouterloot, J. G. A., Wright, M., Yamaguchi, P., Yu, C.-Y., Zeballos, M., Zhang, S., and Ziurys, L. (2019). First M87 Event Horizon Telescope Results. I. The Shadow of the Supermassive Black Hole. , 875(1):L1.

Fan, X., Narayanan, V. K., Lupton, R. H., Strauss, M. A., Knapp, G. R., Becker, R. H., White, R. L., Pentericci, L., Leggett, S. K., Haiman, Z., Gunn, J. E., Ivezić, Ž., Schneider, D. P., Anderson, S. F., Brinkmann, J., Bahcall, N. A., Connolly, A. J., Csabai, I., Doi, M., Fukugita, M., Geballe, T., Grebel, E. K., Harbeck, D., Hennessy, G., Lamb, D. Q., Miknaitis, G., Munn, J. A., Nichol, R., Okamura, S., Pier, J. R., Prada, F., Richards, G. T., Szalay, A., and York, D. G. (2001). A Survey of z>5.8 Quasars in the Sloan Digital Sky Survey. I. Discovery of Three New Quasars and the Spatial Density of Luminous Quasars at z∼6. , 122(6):2833–2849.

Ferrarese, L., Côté, P., Dalla Bontà, E., Peng, E. W., Merritt, D., Jordán, A., Blakeslee, J. P., Haşegan, M., Mei, S., Piatek, S., Tonry, J. L., and West, M. J.

(2006). A Fundamental Relation between Compact Stellar Nuclei, Supermassive Black Holes, and Their Host Galaxies. , 644(1):L21–L24.

Ferrarese, L. and Merritt, D. (2000). A Fundamental Relation between Supermassive Black Holes and Their Host Galaxies. , 539(1):L9–L12.

Filippenko, A. V. and Ho, L. C. (2003). A Low-Mass Central Black Hole in the Bulgeless Seyfert 1 Galaxy NGC 4395. , 588(1):L13–L16.

Fragione, G. and Silk, J. (2020). Repeated mergers and ejection of black holes within nuclear star clusters. *Monthly Notices of the Royal Astronomical Society*, 498(4):4591–4604.

Georgiev, I. Y., Böker, T., Leigh, N., Lützgendorf, N., and Neumayer, N. (2016). Masses and scaling relations for nuclear star clusters, and their co-existence with central black holes. *Monthly Notices of the Royal Astronomical Society*, 457(2):2122–2138.

Georgiev, I. Y., Hilker, M., Puzia, T. H., Goudfrooij, P., and Baumgardt, H. (2009). Globular cluster systems in nearby dwarf galaxies – II. Nuclear star clusters and their relation to massive Galactic globular clusters*. *Monthly Notices of the Royal Astronomical Society*, 396(2):1075–1085.

Graham, A. W. and Spitler, L. R. (2009). Quantifying the coexistence of massive black holes and dense nuclear star clusters. , 397(4):2148–2162.

GRAVITY Collaboration, Abuter, R., Amorim, A., Bauböck, M., Berger, J. P., Bonnet, H., Brandner, W., Clénet, Y., Coudé Du Foresto, V., de Zeeuw, P. T., Deen, C., Dexter, J., Duvert, G., Eckart, A., Eisenhauer, F., Förster Schreiber, N. M., Garcia, P., Gao, F., Gendron, E., Genzel, R., Gillessen, S., Guajardo, P., Habibi, M., Haubois, X., Henning, T., Hippler, S., Horrobin, M., Huber, A., Jiménez-Rosales, A., Jocou, L., Kervella, P., Lacour, S., Lapeyrère, V., Lazareff, B., Le Bouquin, J. B., Léna, P., Lippa, M., Ott, T., Panduro, J., Paumard, T., Perraut, K., Perrin, G., Pfuhl, O., Plewa, P. M., Rabien, S., Rodríguez-Coira, G., Rousset, G., Sternberg, A., Straub, O., Straubmeier, C., Sturm, E., Tacconi, L. J., Vincent, F., von Fellenberg, S., Waisberg, I., Widmann, F., Wieprecht, E., Wiezorrek, E., Woillez, J., and Yazici, S. (2018). Detection of orbital motions near the last stable circular orbit of the massive black hole SgrA*. , 618:L10.

Gültekin, K., Richstone, D. O., Gebhardt, K., Lauer, T. R., Tremaine, S., Aller, M. C., Bender, R., Dressler, A., Faber, S. M., Filippenko, A. V., Green, R., Ho, L. C., Kormendy, J., Magorrian, J., Pinkney, J., and Siopis, C. (2009). The M-σ and M-L Relations in Galactic Bulges, and Determinations of Their Intrinsic Scatter. , 698(1):198–221.

Gürkan, M. A. and Rasio, F. A. (2005). The disruption of stellar clusters containing massive black holes near the galactic center. *The Astrophysical Journal*, 628(1):236.

Haemmerlé, L. (2020). General-relativistic instability in hylotropic supermassive stars. , 644:A154.

Haiman, Z., Abel, T., and Rees, M. J. (2000). The radiative feedback of the first cosmological objects. *The Astrophysical Journal*, 534(1):11–24.

Heggie, D. and Hut, P. (2003). *The Gravitational Million–Body Problem: A Multidisciplinary Approach to Star Cluster Dynamics*. Cambridge University Press.

Heggie, D. C. (1975). Binary evolution in stellar dynamics. , 173:729–787.

Hénon, M. (1961). Sur l'évolution dynamique des amas globulaires. *Annales d'Astrophysique*, 24:369.

Hénon, M. (1975). Two Recent Developments Concerning the Monte Carlo Method. In Hayli, A., editor, *Dynamics of the Solar Systems*, volume 69, page 133.

Hills, J. G. (1975). Effect of binary stars on the dynamical evolution of stellar clusters. II. Analytic evolutionary models. , 80:1075–1080.

Hirano, S., Hosokawa, T., Yoshida, N., Umeda, H., Omukai, K., Chiaki, G., and Yorke, H. W. (2014). iONE HUNDRED FIRST STARS/i: PROTOSTELLAR EVOLUTION AND THE FINAL MASSES. *The Astrophysical Journal*, 781(2):60.

Hlavacek-Larrondo, J., Fabian, A. C., Edge, A. C., and Hogan, M. T. (2012). On the hunt for ultramassive black holes in brightest cluster galaxies. , 424(1):224–231.

Hopman, C. and Alexander, T. (2006). Resonant relaxation near a massive black hole: The stellar distribution and gravitational wave sources. *The Astrophysical Journal*, 645(2):1152.

Hosokawa, T., Yorke, H. W., Inayoshi, K., Omukai, K., and Yoshida, N. (2013). Formation of Primordial Supermassive Stars by Rapid Mass Accretion. , 778(2):178.

Hut, P., McMillan, S., and Romani, R. W. (1992). The Evolution of a Primordial Binary Population in a Globular Cluster. , 389:527.

Inayoshi, K., Hosokawa, T., and Omukai, K. (2013). Pulsational instability of supergiant protostars: do they grow supermassive by accretion? *Monthly Notices of the Royal Astronomical Society*, 431(4):3036–3044.

Inayoshi, K., Visbal, E., and Haiman, Z. (2020). The assembly of the first massive black holes. *Annual Review of Astronomy and Astrophysics*, 58(1):27–97.

Inayoshi, K., Visbal, E., and Haiman, Z. (2020). The Assembly of the First Massive Black Holes. , 58:27–97.

Johnson, J. L. and Bromm, V. (2007). The aftermath of the first stars: massive

black holes. *Monthly Notices of the Royal Astronomical Society*, 374(4):1557–1568.

Khalisi, E. and Spurzem, R. (2014). Latest update: 11.

Kormendy, J. and Richstone, D. (1992). Evidence for a Supermassive Black Hole in NGC 3115. , 393:559.

Koushiappas, S. M., Bullock, J. S., and Dekel, A. (2004). Massive black hole seeds from low angular momentum material. , 354(1):292–304.

Kroupa, P., Subr, L., Jerabkova, T., and Wang, L. (2020). Very high redshift quasars and the rapid emergence of supermassive black holes. , 498(4):5652–5683.

Kupi, G., Amaro-Seoane, P., and Spurzem, R. (2006). Dynamics of compact object clusters: a post-newtonian study. *Monthly Notices of the Royal Astronomical Society: Letters*, 371(1):L45–L49.

Kustaanheimo, P., SCHINZEL, A., DAVENPORT, H., and STIEFEL, E. (1965). Perturbation theory of kepler motion based on spinor regularization. 1965(218):204–219.

Latif, M. A., Schleicher, D. R. G., Schmidt, W., and Niemeyer, J. (2013). Black hole formation in the early Universe. *Monthly Notices of the Royal Astronomical Society*, 433(2):1607–1618.

Leigh, N., Sills, A., and Böker, T. (2013). Modifying two-body relaxation in N-body systems by gas accretion. *Monthly Notices of the Royal Astronomical Society*, 433(3):1958–1965.

Leigh, N. W. C., Giersz, M., Marks, M., Webb, J. J., Hypki, A., Heinke, C. O., Kroupa, P., and Sills, A. (2014). The state of globular clusters at birth – II. Primordial binaries. *Monthly Notices of the Royal Astronomical Society*, 446(1):226–239.

Lupi, A., Colpi, M., Devecchi, B., Galanti, G., and Volonteri, M. (2014). Constraining the high-redshift formation of black hole seeds in nuclear star clusters with gas inflows. , 442(4):3616–3626.

Lynden-Bell, D. and Wood, R. (1968). The gravo-thermal catastrophe in isothermal spheres and the onset of red-giant structure for stellar systems. , 138:495.

Machacek, M. E., Bryan, G. L., and Abel, T. (2001). Simulations of Pregalactic Structure Formation with Radiative Feedback. , 548(2):509–521.

Mackey, A. D., Wilkinson, M. I., Davies, M. B., and Gilmore, G. F. (2007). The effect of stellar-mass black holes on the structural evolution of massive star clusters. *Monthly Notices of the Royal Astronomical Society: Letters*, 379(1):L40–L44.

Makino, J. (1991). Optimal order and time-step criterion for aarseth-type n-body integrators. *Astrophysical Journal; (USA)*, 369.

Makino, J. and Aarseth, S. J. (1992). On a Hermite Integrator with Ahmad-Cohen Scheme for Gravitational Many-Body Problems. , 44:141–151.

Mayer, L., Kazantzidis, S., Escala, A., and Callegari, S. (2010). Direct formation of supermassive black holes via multi-scale gas inflows in galaxy mergers. , 466(7310):1082–1084.

McConnell, N. J., Ma, C.-P., Gebhardt, K., Wright, S. A., Murphy, J. D., Lauer, T. R., Graham, J. R., and Richstone, D. O. (2011). Two ten-billion-solar-mass black holes at the centres of giant elliptical galaxies. , 480(7376):215–218.

Mikkola, S. and Aarseth, S. J. (1998). An efficient integration method for binaries in n-body simulations. *New Astronomy*, 3(5):309–320.

Miller, M. C. and Hamilton, D. P. (2002). Production of intermediate-mass black holes in globular clusters. , 330(1):232–240.

Milosavljević, M., Bromm, V., Couch, S. M., and Oh, S. P. (2009). Accretion onto "seed" black holes in the first galaxies. *The Astrophysical Journal*, 698(1):766.

Neumayer, N., Seth, A., and Böker, T. (2020). Nuclear star clusters. , 28(1):4.

Neumayer, N. and Walcher, C. J. (2012). Are Nuclear Star Clusters the Precursors of Massive Black Holes? *Advances in Astronomy*, 2012:709038.

Nguyen, D. D., Seth, A. C., Neumayer, N., Iguchi, S., Cappellari, M., Strader, J., Chomiuk, L., Tremou, E., Pacucci, F., Nakanishi, K., Bahramian, A., Nguyen, P. M., den Brok, M., Ahn, C. C., Voggel, K. T., Kacharov, N., Tsukui, T., Ly, C. K., Dumont, A., and Pechetti, R. (2019). Improved Dynamical Constraints on the Masses of the Central Black Holes in Nearby Low-mass Early-type Galactic Nuclei and the First Black Hole Determination for NGC 205. , 872(1):104.

Nguyen, D. D., Seth, A. C., Neumayer, N., Kamann, S., Voggel, K. T., Cappellari, M., Picotti, A., Nguyen, P. M., Böker, T., Debattista, V., Caldwell, N., McDermid, R., Bastian, N., Ahn, C. C., and Pechetti, R. (2018). Nearby Early-type Galactic Nuclei at High Resolution: Dynamical Black Hole and Nuclear Star Cluster Mass Measurements. , 858(2):118.

Omukai, K. (2001). Primordial star formation under far-ultraviolet radiation. *The Astrophysical Journal*, 546(2):635–651.

Omukai, K., Schneider, R., and Haiman, Z. (2008). Can Supermassive Black Holes Form in Metal-enriched High-Redshift Protogalaxies? , 686(2):801–814.

O'Shea, B. W. and Norman, M. L. (2008). Population III Star Formation in a Λ CDM Universe. II. Effects of a Photodissociating Background. , 673(1):14–33.

Perna, R., Wang, Y.-H., Farr, W. M., Leigh, N., and Cantiello, M. (2019).

Constraining the black hole initial mass function with LIGO/virgo observations. *The Astrophysical Journal*, 878(1):L1.

Peters, P. C. (1964). Gravitational Radiation and the Motion of Two Point Masses. *Physical Review*, 136(4B):1224–1232.

Plummer, H. C. (1911). On the problem of distribution in globular star clusters. , 71:460–470.

Portegies Zwart, S. F., Baumgardt, H., Hut, P., Makino, J., and McMillan, S. L. W. (2004). Formation of massive black holes through runaway collisions in dense young star clusters. , 428(6984):724–726.

Rees, M. J. (1984). Black Hole Models for Active Galactic Nuclei. , 22:471–506.

Regan, J. A. and Downes, T. P. (2018). Fragmentation inside atomic cooling haloes exposed to Lyman–Werner radiation. *Monthly Notices of the Royal Astronomical Society*, 475(4):4636–4647.

Reinoso, B., Schleicher, D. R. G., Fellhauer, M., Klessen, R. S., and Boekholt, T. C. N. (2018). Collisions in primordial star clusters. Formation pathway for intermediate mass black holes. , 614:A14.

Reinoso, B., Schleicher, D. R. G., Fellhauer, M., Leigh, N. W. C., and Klessen, R. S. (2020). The effects of a background potential in star cluster evolution: a delay in the relaxation time-scale and runaway collision processes.

Reisswig, C., Ott, C. D., Abdikamalov, E., Haas, R., Mösta, P., and Schnetter, E. (2013). Formation and coalescence of cosmological supermassive-black-hole binaries in supermassive-star collapse. *Physical Review Letters*, 111(15).

Richstone, D., Bower, G., and Dressler, A. (1990). Constraints on the Mass Distribution near the Centers of M31 and M32. , 353:118.

Rossa, J., van der Marel, R. P., Böker, T., Gerssen, J., Ho, L. C., Rix, H.-W., Shields, J. C., and Walcher, C.-J. (2006). Hubble Space Telescope STIS Spectra of Nuclear Star Clusters in Spiral Galaxies: Dependence of Age and Mass on Hubble Type. , 132(3):1074–1099.

Schleicher, D. R. G., Palla, F., Ferrara, A., Galli, D., and Latif, M. (2013). Massive black hole factories: Supermassive and quasi-star formation in primordial halos. , 558:A59.

Sedda, M. A. (2020). Birth, life, and death of black hole binaries around supermassive black holes: Dynamical evolution of gravitational wave sources. *The Astrophysical Journal*, 891(1):47.

Seth, A., Agüeros, M., Lee, D., and Basu-Zych, A. (2008). The Coincidence of Nuclear Star Clusters and Active Galactic Nuclei. , 678(1):116–130.

Shang, C., Bryan, G. L., and Haiman, Z. (2010). Supermassive black hole formation

by direct collapse: keeping protogalactic gas H_2 free in dark matter haloes with virial temperatures T_{vir} > rsim 10^4 K. , 402(2):1249–1262.

Shankar, F., Crocce, M., Miralda-Escudé, J., Fosalba, P., and Weinberg, D. H. (2010). On the Radiative Efficiencies, Eddington Ratios, and Duty Cycles of Luminous High-redshift Quasars. , 718(1):231–250.

Shibata, M. and Shapiro, S. L. (2002). Collapse of a Rotating Supermassive Star to a Supermassive Black Hole: Fully Relativistic Simulations. , 572(1):L39–L43.

Soffel, M. H. (1989). *Relativity in Astrometry, Celestial Mechanics and Geodesy*, pages 1–31. Springer Berlin Heidelberg, Berlin, Heidelberg.

Spitzer, L. (1987). *Dynamical evolution of globular clusters.*

Tagawa, H., Haiman, Z., and Kocsis, B. (2020). Formation and evolution of compact-object binaries in agn disks. *The Astrophysical Journal*, 898(1):25.

Tonry, J. L. (1984). Constraints on the orbits of multiple nuclei in brightest cluster galaxies. , 279:13–18.

Tremaine, S., Gebhardt, K., Bender, R., Bower, G., Dressler, A., Faber, S. M., Filippenko, A. V., Green, R., Grillmair, C., Ho, L. C., Kormendy, J., Lauer, T. R., Magorrian, J., Pinkney, J., and Richstone, D. (2002). The Slope of the Black Hole Mass versus Velocity Dispersion Correlation. , 574(2):740–753.

van der Marel, R. P., Rix, H. W., Carter, D., Franx, M., White, S. D. M., and de Zeeuw, T. (1994). Velocity profiles of galaxies with claimed black holes - I. Observations of M 31, M 32, NGC 3115 and NGC 4594. , 268:521–543.

Vergara, M. C., Escala, A., Schleicher, D. R. G., and Reinoso, B. (2022). Global instability by runaway collisions in nuclear stellar clusters: Numerical tests of a route for massive black hole formation. *arXiv e-prints*, page arXiv:2209.15066.

Verolme, E. K., Cappellari, M., Copin, Y., van der Marel, R. P., Bacon, R., Bureau, M., Davies, R. L., Miller, B. M., and de Zeeuw, P. T. (2002). A SAURON study of M32: measuring the intrinsic flattening and the central black hole mass. , 335(3):517–525.

Wang, L., Spurzem, R., Aarseth, S., Nitadori, K., Berczik, P., Kouwenhoven, M. B. N., and Naab, T. (2015). nbody6++gpu: ready for the gravitational million-body problem. *Monthly Notices of the Royal Astronomical Society*, 450(4):4070–4080.

Wehner, E. H. and Harris, W. E. (2006). From Supermassive Black Holes to Dwarf Elliptical Nuclei: A Mass Continuum. , 644(1):L17–L20.

Whalen, D., O'Shea, B. W., Smidt, J., and Norman, M. L. (2008). How the First Stars Regulated Local Star Formation. I. Radiative Feedback. , 679(2):925–941.

Wise, J. H., Turk, M. J., and Abel, T. (2008). Resolving the formation of

protogalaxies. II. central gravitational collapse. *The Astrophysical Journal*, 682(2):745–757.

Wu, X.-B., Wang, F., Fan, X., Yi, W., Zuo, W., Bian, F., Jiang, L., McGreer, I. D., Wang, R., Yang, J., Yang, Q., Thompson, D., and Beletsky, Y. (2015). An ultraluminous quasar with a twelve-billion-solar-mass black hole at redshift 6.30. , 518(7540):512–515.

Yoshida, N., Omukai, K., Hernquist, L., and Abel, T. (2006). Formation of primordial stars in a λ cdm universe. *The Astrophysical Journal*, 652(1):6–25.

Zwart, S. F. P. and McMillan, S. L. W. (2002). The runaway growth of intermediate-mass black holes in dense star clusters. *The Astrophysical Journal*, 576(2):899.